Asymptotic gravitational wave fluxes from a spinning particle in circular equatorial orbits around a rotating black hole

Enno Harms,[1] Georgios Lukes-Gerakopoulos,[2] Sebastiano Bernuzzi,[3] and Alessandro Nagar[4]

[1]*Theoretical Physics Institute, University of Jena, 07743 Jena, Germany*
[2]*Institute of Theoretical Physics, Faculty of Mathematics and Physics, Charles University in Prague,
18000 Prague, Czech Republic*
[3]*DiFeST, University of Parma, and INFN, 43124 Parma, Italy*
[4]*Institut des Hautes Etudes Scientifiques, 91440 Bures-sur-Yvette, France*

We present a new computation of the asymptotic gravitational wave energy fluxes emitted by a *spinning* particle in circular equatorial orbits about a Kerr black hole. The particle dynamics is computed in the pole-dipole approximation, solving the Mathisson-Papapetrou equations with the Tulczyjew spin-supplementary-condition. The fluxes are computed, for the first time, by solving the $2 + 1$ Teukolsky equation in the time-domain using hyperboloidal and horizon-penetrating coordinates. Denoting by M the black hole mass and by μ the particle mass, we cover dimensionless background spins $a/M = (0, \pm 0.9)$ and dimensionless particle spins $-0.9 \leq S/\mu^2 \leq +0.9$. Our results span orbits of Boyer-Lindquist coordinate radii $4 \leq r/M \leq 30$; notably, we investigate the strong-field regime, in some cases even beyond the last-stable-orbit. We compare our numerical results for the gravitational wave fluxes with the 2.5th order accurate post-Newtonian (PN) prediction obtained analytically by Tanaka *et al.* [Phys. Rev. D 54, 3762 (1996)]: we find an unambiguous trend of the PN-prediction toward the numerical results when r is large. At $r/M = 30$ the fractional agreement between the full numerical flux, approximated as the sum over the modes $m = 1, 2, 3$, and the PN prediction is $\lesssim 0.5\%$ in all cases tested. This is close to our fractional numerical accuracy ($\sim 0.2\%$). For smaller radii, the agreement between the 2.5PN prediction and the numerical result progressively deteriorates, as expected. Our numerical data will be essential to develop suitably resummed expressions of PN-analytical fluxes in order to improve their accuracy in the strong-field regime.

I. INTRODUCTION

The black hole (BH) binary problem is one of the most interesting topics of numerical relativity due to its relevance for gravitational wave (GW) detection and its enormous numerical challenges. In the test-particle limit we assume that one of the two companions has such a small mass $\mu \ll M$, where M is the mass of the big companion, that the system can be modeled as a fixed BH background plus a perturbation. Thus, linearized equations like the Regge-Wheeler-Zerilli (RWZ) equations [1,2] and the Teukolsky equation (TE) [3,4] can be used. The particle limit is relevant in its own right as the extreme-mass-ratio (EMR) corner of parameter space [5,6], but even more important because, (i) the underlying physics are the same at any mass-ratio, which allows us to connect the particle results to comparable mass ratios; in some cases qualitatively [7], in other cases even quantitatively [8], (ii) semianalytical models like the effective-one-body (EOB) model rely on EMR information, see, e.g., [9], (iii) the physical origin of experimental observations can be disentangled with more intuition; e.g., a clean definition of the trajectory or the couplings of orbital and spin angular momenta is possible, and (iv) the computational costs are negligible in contrast to

full-fledged numerical relativity (NR) simulations like, e.g., [10]. Hence, it is highly desirable to have tools like a "point-particle laboratory"; in particular, one that allows us to study the effects of spin-spin-couplings and spin-orbit couplings on the gravitational waveforms.

The treatment of point particles with spin has a long history in relativity [11–13]. A major step was Mathisson's model of a "gravitational skeleton" [14] (see also [15,16]), in which the energy momentum tensor of a spinning body is expanded into its multipolar moments. Assuming that the body be sufficiently small, one can neglect higher multipole moments; e.g., restricting to the mass (monopole) and linear spin effects (dipole) one obtains the well-known "pole-dipole" approximation. Within this framework and using the conservation equation $\nabla_\mu T^{\mu\nu} = 0$, Papapetrou derived his famous equations of motion (EoM) for a spinning particle [17,18]. The nowadays standard form of these equations was obtained in a series of subsequent works by Tulczyjew [15], Dixon [19–22] and Wald [23], and it is written in terms of the world line variables $\{v^\mu, p^\mu, S^{\mu\nu}\}$, i.e. the tangent vector, the linear four momentum and the spin tensor respectively. In this form the equations are often referred to as the "Mathisson-Papapetrou-Dixon" equations (MPEQs), emphasizing the

important early contribution of Mathisson [14] and the later reformulations of Dixon. As discussed already by Papapetrou, the EoM contain three degrees of freedom that have to be fixed in order to close the system of ordinary differential equations. This freedom can be interpreted as the arbitrariness in the choice of the reference point inside the spinning body that shall be tracked by the EoM. The reference point is not unique because any spinning body has a lower bound for its size: $R \gtrsim S/\mu$, where R is its radius, S its spin magnitude and μ its mass [24]. Thus, the MPEQs have to be understood as describing a small but not pointlike body [23], and, in principle, one could choose any point inside the body as the reference point that follows the EoM. A unique choice in classical mechanics would be the center of mass, which, however, in GR is observer dependent [25] (see [16] for a nice visualization). It is conventional to use the center of mass with respect to which the "spin" of the body is defined as the reference point tracked by the world line $X^{\mu}(\lambda)$, with λ the proper time. Thus, a condition that fixes the spin also fixes the reference point traced by $X^{\mu}(\lambda)$, and the freedom in the EoM can be removed by imposing a spin-supplementary condition (SSC). Several such SSCs have been proposed in the literature [15,18,19,26–29], usually by demanding the reference-point to coincide with the center-of-mass as perceived by some preferred timelike observer and, consequently, with the spin to be orthogonal to this observer's direction of motion.

Over the years the dynamics of a pole-dipole particle was studied in great detail within the Mathisson-Papapetrou framework and under the influence of different SSCs, see, e.g., [29–33] for an overview. Note, that technically the "gravitational skeleton" can be used to derive EoM at any multipolar order and especially second (quadrupole) moments modeled as quadratic in spin effects have already been included in many recent works, see, e.g., [16,22,34–39]. On the contrary, the literature on GWs emitted by spinning particles that move in BH spacetimes is rather sparse; probably, due to the fact that the interest in the topic is mostly theoretical. Estimates on the honest effect of the spin of the particle predict at best secular relevance in intermediate-mass-ratios [30,40]. Therefore, it does not come as a surprise that all studies mentioned below went beyond the range of astrophysically realistic values for the spins (see Ch. II, Sec. 3B in [32]). This is motivated by the hope that high spin values can nonetheless provide very valuable theoretical information.

Almost 20 years ago Mino *et al.* [41] performed first numerical studies of the GW emission from a spinning particle on radial plunges along the rotation axis of a Kerr BH by solving the TE in the frequency domain, more precisely within the Sasaki-Nakamura formalism [42]. The work of Mino *et al.* [41] was complemented by radial plunges in the equatorial plane, as considered by Saijo *et al.* in [43]. Recently, Han [44] computed numerically energy

fluxes of a spinning particle in circular, equatorial orbit about a rotating Kerr BH, both to infinity and down the horizon, using the same approach in the frequency-domain. In a somewhat different approach, using metric perturbations and linearizing the Einstein equations, Tominaga *et al.* [45,46] investigated GWs from a spinning particle moving in the spherically symmetric background created by a neutron star. In 2015, Burko and Khanna [47] studied the effect of the particle spin on the waveforms produced along circular motion around a Schwarzschild BH and found that it can be as important as conservative self-force effects. All the studies mentioned so far, restricted the spin of the central BH, here denoted $\vec{S}_1$, and the spin of the small body, $\vec{S}_2$, to be (anti-)parallel—and we will do so, as well. On the analytical side, post-Newtonian (PN) calculations for spinning binaries of comparable masses were performed in [48–50] and in several works since, see [16] for an overview. In the point particle limit, Tanaka *et al.* [51] computed energy fluxes to infinity at 2.5PN by solving the Sasaki-Nakamura equations. Their results, Eqs. (5.17) and Eqs. (5.19) in [51], comprise the next-to-leading-order (NLO) in the spin-orbit interaction and the leading-order (LO) in the spin-square interaction and will serve as the target solutions for our study. Recently, new analytical expressions for the fluxes became available at higher PN accuracy (in both the spin-orbit and the spin-spin interaction), remarkably in the comparable-mass case: spin-orbit contributions to the flux were obtained at next-to-next-to-leading order in Ref. [52,53], see also [54,55], while spin-square terms were given at NLO in Ref. [56], notably also with the addition of the 4PN tail contribution [57].

For simplicity, here we choose to not include the test-particle limit of the analytical expression of Refs. [53,56], i.e. we only rely on the 2.5PN accurate original expression of Tanaka *et al.* [51]. The higher-order PN terms will be included, in a suitably factorized and resummed form [58], in a follow-up work that aims at assessing in detail the accuracy of the analytical expressions in the strong-field regime.

In this work we will solve the MPEQs with the Tulczyjew-SSC (see below) for circular equatorial orbits, using a variational Gauss-Runge-Kutta integration scheme as presented in [59]. The obtained dynamics will be fed to a time-domain Teukolsky solver, which was successfully used in the computation of tail decay rates [60] and GWs from EOB-radiation-reaction-driven particle inspirals [61,62]. The obtained GWs are used to compute energy fluxes to infinity. We compare our numerical data against the 2.5PN result of Tanaka *et al.* [51]. We will prove that our data approach toward the PN-prediction as $r \to \infty$ until the differences reach the level of our numerical uncertainty estimate, which thus mutually confirms both our numerical implementation and the analytical PN calculation of Tanaka *et al.* (also

the test-particle limit of the comparable-mass PN calculation of [52,54,55,57]). Moreover, we will set up a database with numerical values for the infinity fluxes, which will serve as an orientation for future studies and, in particular, allow us to assess the success of manipulations in the analytical formulas. Note that in the nonspinning case the PN-results have been successfully processed in [63–65] with resummation techniques in order to extend the range of accuracy toward the strong-field regime.

The paper is organized as follows. In Sec. II we will shortly describe the MPEQs and the procedure of finding circular orbits. In Sec. III we review the TE and our approach to solving it numerically in the time-domain. In addition, we present our strategy of computing the TE source term with spin and the implementation in the Teukode. Notably, our code is, to the best of our knowledge, the first one to solve the TE in the time-domain with a source term for a spinning particle. In Sec. IV a discussion of our numerical results for the total energy fluxes of a spinning particle is given, with respect to the analytical 2.5PN prediction. Finally, in Appendix A we complement the consistency checks of our numerics with (i) an analysis of the multipolarly decomposed fluxes, (ii) repeating the comparison for the total flux with respect to a different PN variable than that used in the main body, and (iii) a comparison against the numerical results of [44]. In Appendix B we collect our results in tables, as a reference for future studies.

We use geometric units, $c = G = 1$, and the Riemann tensor defined as $R^\alpha{}_{\beta\gamma\delta} = \Gamma^\alpha_{\gamma\lambda}\Gamma^\lambda_{\delta\beta} - \partial_\delta\Gamma^\alpha_{\gamma\beta} - \Gamma^\alpha_{\delta\lambda}\Gamma^\lambda_{\gamma\beta} + \partial_\gamma\Gamma^\alpha_{\delta\beta}$, where the Christoffel symbols Γ are computed from the metric with signature $(-, +, +, +)$. We often employ reduced variables as denoted with a hat; e.g., $\hat{r} = r/M$ and $\hat{a} = a/M = \pm|\vec{S}_1|/M^2$, where $\vec{S}_1$ is the angular momentum, M the mass of the central BH and the $+(-)$ is chosen when $\vec{S}_1$ is aligned (antialigned) with the strictly positive orbital angular momentum. The spin of the particle is expressed here, as well as in most of the literature on this subject, with the dimensionless quantity $\sigma = S/(\mu M) = \pm|\vec{S}_2|/(\mu M)$, where $\vec{S}_2$ is the spin angular momentum of the particle and μ its conserved mass. If we think of the particle as a model of a BH, its maximal spin angular momentum would be $S = \pm\mu^2$ (see [32] for a discussion on maximal spins of stellar objects), which means σ would be restricted to $-\nu \leq \sigma \leq \nu$, with $\nu \equiv \mu/M$, that is $-1 \leq \sigma/\nu \leq 1$ (see also [66] for a related discussion). In practice, we use $M = \mu = 1$ in our numerics, avoiding the inconvenient appearance of factors ν and restricting our spin parameter to $\sigma \in [-1, 1]$. This setting is somewhat counterintuitive to the condition $\mu \ll M$, which we assume in doing perturbation theory, but since μ and M are just scales in the used equations we are free to use the most convenient values numerically.

II. DYNAMICS OF A POLE-DIPOLE PARTICLE

In this section we briefly recall the EoM for a pole-dipole particle and explain our choice for the SSC. More details on the used numerical integration scheme can be found in [59], where one of us compared the dynamics of the MPEQs with the EoM of the Hamiltonian for a spinning particle [67]. In addition, we will outline the procedure for finding initial data that leads to circular equatorial orbits (CEOs), including unstable ones. We mention that, equivalently, the dynamics for a pole-dipole particle under the TUL-SSC which moves on a circular orbit in the equatorial plane with (anti)aligned spin can be computed analytically following the Appendix of [51].

A. Equations of motion and the spin-supplementary condition

The MPEQs have been the object of many studies, see, e.g., [30] for a review and [68–70] for recent works. In the nowadays standard form they read

$$v^\alpha\nabla_\alpha p^\mu = -\frac{1}{2}R^\mu{}_{\nu\rho\sigma}v^\nu S^{\rho\sigma}$$
$$v^\alpha\nabla_\alpha S^{\mu\nu} = p^\mu v^\nu - p^\nu v^\mu, \tag{1}$$

where $v^\mu = dX^\mu/d\lambda$ is the tangent vector to the world line $X^\mu(\lambda)$, with λ the proper time, of a yet unspecified reference point inside the spinning body and p^μ its total linear four-momentum. The spin tensor $S^{\mu\nu}$ is defined in some analogy to classical spin angular momentum via spatial integrals over the stress-energy tensor $T^{\mu\nu}$ on a given hypersurface and with respect to the chosen reference point [29,32]. The more intuitive picture of spin as a three-dimensional vector can be partially retrieved after the reference point is fixed through a SSC (see below). Independently from the SSC, any background symmetry implies a constant of motion with respect to evolution upon the MPEQs. Namely, for a Killing vector ξ^μ the quantity

$$C = \xi^\mu p_\mu - \frac{1}{2}\xi_{\mu;\nu}S^{\mu\nu} \tag{2}$$

remains conserved upon evolution.

As mentioned earlier, the system of Eqs. (1) contains three degrees of freedom associated with the arbitrariness of the tracked reference point and thus with the notion of *spin*. This arbitrariness has to be removed before one can use Eqs. (1) to find dynamics of a pole-dipole particle. Here, we choose to close the system with the "Tulczyjew-SSC" [15] (TUL-SSC)

$$S^{\mu\nu}p_\mu = 0, \tag{3}$$

which is known to feature conservation of the dynamical rest mass $\mu := \sqrt{-p^\mu p_\mu}$ and of the spin magnitude

$$S^2 = \frac{1}{2} S^{\mu\nu} S_{\mu\nu}. \tag{4}$$

Note that all previous numerical studies on the topic of energy fluxes from spinning particles made the same choice [41,43,44,51]. For the TUL-SSC a spin four-vector is defined as

$$S_\mu = -\frac{1}{2} \epsilon_{\mu\nu\rho\sigma} u^\nu S^{\rho\sigma}, \tag{5}$$

where $u^\nu := p^\nu/\mu$ is the specific four momentum, $\epsilon_{\mu\nu\rho\sigma} = \sqrt{-g}\tilde{\epsilon}_{\mu\nu\rho\sigma}$ is the Levi-Civita tensor with the Levi-Civita symbol $\tilde{\epsilon}_{0123} = 1$ and g is the determinant of the background metric tensor. Equation (5) can be rearranged to get

$$S^{\rho\sigma} = -\epsilon^{\rho\sigma\gamma\delta} S_\gamma u_\delta. \tag{6}$$

Substituting Eq. (6) into the definition of the spin-magnitude, Eq. (4), we get that the spin magnitude can be written in terms of the four-vector

$$S^2 = S^\mu S_\mu. \tag{7}$$

The TUL-SSC by construction implies the orthogonality of the spin-vector and the linear momentum four-vector, $S_\mu p^\mu = 0$, and it has been shown that $S_\mu v^\mu = 0$ holds as well, see, e.g., [68].

In general, the imposition of a SSC closes the system of evolution equations for the world line variables $\{v^\mu, p^\mu, S^{\mu\nu}\}$. For the TUL-SSC one can deduce an explicit relation $v^\mu(u^\mu, S^{\mu\nu})$; namely,

$$v^\mu = \frac{\mathsf{m}}{\mu} \left(u^\mu + \frac{2 S^{\mu\nu} R_{\nu\rho\kappa\lambda} u^\rho S^{\kappa\lambda}}{4\mu^2 + R_{\alpha\beta\gamma\delta} S^{\alpha\beta} S^{\gamma\delta}} \right), \tag{8}$$

where $\mathsf{m} = -p_\mu v^\mu$ is the rest mass with respect to v^μ, which for the TUL-SSC is only conserved up to linear order in S. In practice, the value of m is set such that the tangent to the world line satisfies the condition $v^\mu v_\mu = -1$. Interestingly, relation (8) does not, in general, obey $v^\mu \| u^\mu$ but rather $v^\mu = u^\mu + \mathcal{O}(S^2)$, i.e. the specific linear momentum and the tangent vector differ by a quadratic-in-spin term. We mention that the relevant literature [41,43,44,51] that we use for comparisons also uses the TUL-SSC.

Here, it is useful to comment on the implications of the quadratic-in-spin term introduced to the system by virtue of the TUL-SSC. The region of interest in this paper is the weak-field, where $R_{\alpha\beta\gamma\delta} \approx 0$ so that the spin-square term in Eq. (8) is suppressed and our dynamics remain basically linear-in-spin (which directly reflects in the obtained GW fluxes). Instead, in the strong-field and at large spin values $\sigma \sim \mathcal{O}(1)$ the $\mathcal{O}(S^2)$-terms have a relevant influence on the dynamics [71]. Let us briefly discuss what this entails for

the significance of our study in the strong-field; especially, with respect to the question of how reliable our results might be for more realistic bodies with a *small* but nonvanishing quadrupolar moment. The very first assumption of the pole-dipole model is that the energy-momentum tensor of the body that we aim to model is assumed to exhibit only zeroth and first moments when subjected to a multipolar expansion. When this assumption is strictly satisfied, the maintenance of the $\mathcal{O}(S^2)$-terms introduced by the TUL-SSC is fully compatible with the pole-dipole approximation. On the contrary, if one was to stretch the limits of the model beyond a rigorous description, by considering a realistic body for which the assumption of vanishing higher multipole moments is violated to a small extent, the pole-dipole approach becomes *ab initio* an approximation which neglects quadratic-in-spin terms (because in realistic bodies the spin induces a quadrupole moment which is described as a spin-square term [16,72,73]). Thus, for such bodies the pole-dipole dynamics can only give a qualitative description of the leading-order in S behavior. To at least consistently investigate this leading-order in S influence on the motion, one would have to neglect quadratic-in-spin terms all over, also in Eq. (8). In the future, we plan on doing so by repeating our analysis with the MPEQs linearized in the spin in order to have dynamics which are fully consistent for realistic bodies also in the strong-field (though restricted to linear order in the spin).

In summary, we have decided to solve the full quadratic-in-spin relation, Eq. (8). Thus, our dynamics is rigorous, also in the strong-field, as long as the considered body can in fact be described only by its monopole and dipole. Instead, bodies with a small but nonvanishing quadrupole moment are only in the weak-field consistently described by our dynamics—and only at leading order in S; in the strong-field, the sustained $\mathcal{O}(S^2)$-term in the dynamics is inconsistent for such realistic bodies. Astrophysically relevant objects like BHs in a binary are in general not consistently described by our dynamics at small orbital distances because we neglect the expected nonvanishing quadrupolar moments that are induced by the spin and by tidal deformations, see, e.g., [74]. Before applying our results to modeling fluxes from realistic bodies in the strong-field, one would thus need to repeat our analysis with consistent, linear-in-spin dynamics to estimate the influence of the $\mathcal{O}(S^2)$-term. Fortunately, for $\sigma \ll 1$ the discussion is anyway redundant because in that case one can at any rate neglect all quadratic-in-spin terms; in particular, as already argued by Tulczyjew [15,19], one would then linearize Eq. (8), which is frequently seen in analytical approaches like [66,75].

B. The Kerr spacetime background

The Kerr spacetime in Boyer-Lindquist (BL) coordinates (t, r, θ, ϕ) reads

$$ds^2 = g_{tt}dt^2 + 2g_{t\phi}dtd\phi + g_{\phi\phi}d\phi^2$$
$$+ g_{rr}dr^2 + g_{\theta\theta}d\theta^2, \qquad (9)$$

where

$$g_{tt} = -1 + \frac{2Mr}{\Sigma},$$

$$g_{t\phi} = -\frac{2aMr\sin^2\theta}{\Sigma},$$

$$g_{\phi\phi} = \frac{\Lambda\sin^2\theta}{\Sigma},$$

$$g_{rr} = \frac{\Sigma}{\Delta},$$

$$g_{\theta\theta} = \Sigma, \qquad (10)$$

and

$$\Sigma = r^2 + a^2\cos^2\theta,$$

$$\Delta = \varpi^2 - 2Mr,$$

$$\varpi^2 = r^2 + a^2,$$

$$\Lambda = \varpi^4 - a^2\Delta\sin^2\theta. \qquad (11)$$

For a stationary and axisymmetric background like the Kerr one, we have two Killing vector fields, $\xi^\mu_{(t)} = \delta^\mu_t$ and $\xi^\mu_{(\phi)} = \delta^\mu_\phi$ respectively. The first Killing vector provides the conserved energy

$$E = -p_t + \frac{1}{2}g_{t\mu,\nu}S^{\mu\nu}, \qquad (12)$$

while the latter provides the conserved component along the symmetry axis z of the total angular momentum,

$$J_z = p_\phi - \frac{1}{2}g_{\phi\mu,\nu}S^{\mu\nu}. \qquad (13)$$

C. Circular equatorial orbits

The procedure to find circular equatorial orbits (CEO) for a spinning particle on the Kerr spacetime background follows the guidelines given in [68]. Namely, it is assumed that the only nonzero component of the spin vector (5) is the polar one, i.e.,

$$S^\mu = S^\theta\delta^\mu_\theta, \qquad (14)$$

This assumption together with the orthogonality conditions $S_\mu p^\mu = 0$, $S_a v^\mu = 0$ leads to

$$p^\theta = v^\theta = 0. \qquad (15)$$

Since $v^\theta = 0$, we can choose to stay on the equatorial plane, i.e., $\theta = \pi/2$. The condition (14) on the equatorial

plane means that the spin of the particle is parallel to the spin of the central black hole. For $aS > 0$ the spins of the binary are aligned while for $aS < 0$ the spins are antialigned.

From Eqs. (7) and (14) we get $S_\theta = -\sqrt{g_{\theta\theta}}S$. The only nonzero components of the spin tensor computed from Eq. (6) are

$$S^{tr} = -Su_\phi\sqrt{-\frac{g_{\theta\theta}}{g}} = -S^{rt},$$

$$S^{t\phi} = Su_r\sqrt{-\frac{g_{\theta\theta}}{g}} = -S^{\phi t},$$

$$S^{r\phi} = -Su_t\sqrt{-\frac{g_{\theta\theta}}{g}} = -S^{\phi r}. \qquad (16)$$

We can express p_t and p_ϕ as functions of the energy E and of the z-component of the total angular momentum, J_z, by using Eqs. (12) and (13), and, since the system is constrained to the equatorial plane, we get

$$p_t = \frac{-E - \frac{MS}{\mu r^3}(aE - J_z)}{1 - \frac{MS^2}{\mu^2 r^3}},$$

$$p_\phi = \frac{J_z - \frac{aMS}{\mu r^3}[(-1 + \frac{r^3}{a^2 M})aE + J_z]}{1 - \frac{MS^2}{\mu^2 r^3}}, \qquad (17)$$

cf. Eqs. (40) and (41) in [68] [our definitions of E and J_z, Eqs. (12) and (13), differ from those of [68], Eqs. (37) and (38), by a minus sign]. Rewriting the above expressions in dimensionless quantities, we have

$$u_t = \frac{-\hat{E} - \frac{\sigma}{\hat{r}^3}(\hat{a}\,\hat{E} - \hat{J}_z)}{1 - \frac{\sigma^2}{\hat{r}^3}},$$

$$u_\phi = M\frac{\hat{J}_z - \frac{\hat{a}\sigma}{\hat{r}^3}[(-1 + \frac{\hat{r}^3}{\hat{a}^2})\hat{a}\,\hat{E} + \hat{J}_z]}{1 - \frac{\sigma^2}{\hat{r}^3}}, \qquad (18)$$

where $\hat{J}_z := J_z/(\mu M)$, and $\hat{E} := E/\mu$.

From Eq. (8) and Eq. (18) we can get the radial velocity as a function of the dimensionless quantities as well, i.e.,

$$\frac{d\hat{r}}{d\hat{\lambda}} = \frac{(\sigma^2 - \hat{r}^3)\sqrt{V_{\text{eff}}}}{\hat{r}\sqrt{Q}}, \qquad (19)$$

where $\hat{\lambda} = \lambda/M$,

$$Q = \hat{r}^{12} - 4\hat{r}^9\sigma^2 - 6\hat{r}^7\sigma^2(\hat{J}_z - \hat{E}(\hat{a} + \sigma))^2$$
$$+ 6\hat{r}^6\sigma^4 - 3\hat{r}^4\sigma^4(\hat{J}_z - \hat{E}(\hat{a} + \sigma))^2 - 4\hat{r}^3\sigma^6 + \sigma^8,$$

and the effective potential

$$V_{\text{eff}} = (\hat{E}^2 - 1)\hat{r}^8 + 2\hat{r}^7 + \hat{r}^6[\hat{a}^2(\hat{E}^2 - 1) - (\hat{E}\sigma - \hat{J}_z)^2] + 2\hat{r}^5[\hat{a}\,\hat{E}(\hat{a}\,\hat{E} + 3\hat{E}\sigma - 2\hat{J}_z) + (\hat{E}\sigma - \hat{J}_z)^2 + \sigma(\sigma - \hat{E}\hat{J}_z)]$$
$$- 4\hat{r}^4\sigma^2 + 2\hat{a}\sigma\hat{r}^3[(\hat{a}^2 + \hat{a}\sigma)\hat{E}^2 - \hat{E}\hat{J}_z(\sigma + 2\hat{a}) + \hat{a}\sigma + \hat{J}_z^2] + \hat{r}^2\sigma^2[(\hat{a}\,\hat{E} - \hat{J}_z)^2 - \sigma^2] + 2\hat{r}\sigma^4 - \hat{a}^2\sigma^4. \quad (20)$$

The turning points of the radial motion, defined by $V_{\text{eff}} = 0$, provide the first condition to obtain CEOs. The second condition is to demand that there is no radial acceleration. Altogether,

$$V_{\text{eff}} = 0, \qquad \frac{dV_{\text{eff}}}{d\hat{r}} = 0, \quad (21)$$

have to be fulfilled for a CEO. By solving the system of Eqs. (21) for a given radial distance $\hat{r}$ and spin σ we get the energy $\hat{E}$, and the component of the total angular momentum $\hat{J}_z$. If $\frac{d^2 V_{\text{eff}}}{d\hat{r}^2} < 0$, the CEO is stable along the radial direction while, if $\frac{d^2 V_{\text{eff}}}{d\hat{r}^2} > 0$, the CEO is unstable. In the latter case, we have to impose in the code that the radial and the polar velocity are zero during the whole evolution of the system, otherwise small numerical instabilities will drive the numerical trajectory off the CEO. For all values of the (background and particle) spins considered in this work, we computed the radius of the last stable orbit (LSO) by demanding $\frac{d^2}{d\hat{r}^2} V_{\text{eff}} = 0$ in addition to Eqs. (21) (see e.g. [68,76] for the same calculation). The corresponding

numbers are listed in Table I, together with the respective orbital frequency of the particle as computed from Eq. (22).

D. Orbital configurations

We consider orbits with Boyer-Lindquist radii $\hat{r} = \{5, 6, 7, 8, 10, 12, 15, 20\}$. For some configurations, further data points at $\hat{r} = 4$ and $\hat{r} = 30$ are computed. Comparing with Table I, this means we are considering also unstable orbits beyond the LSO. For each value of $\hat{r}$ we consider three values of the background spin $\hat{a} = \{-0.9, 0, +0.9\}$ and ten values of the particle spin $\sigma = \{-0.9, -0.7, -0.5, -0.3, -0.1, +0.1, +0.3, +0.5, +0.7, +0.9\}$.

After obtaining the corresponding initial data following Sec. II C, we numerically integrate the EoM, Eq. (1) and Eq. (8). As an immediate check of our dynamics we compare the obtained numerical frequency $\Omega^{\text{Num}} = v^\phi/v^t$ with the exact analytical expression, Eq. (12) in [44], that generalizes the usual Kepler law from geodesic motion to our EoM for a spinning particle (cf. also the Appendix of [51], which gives a procedure to compute the frequency as well). Within our notation, this (dimensionless) orbital frequency reads

$$\hat{\Omega} \equiv M\Omega = \frac{\hat{a} + \sigma(\frac{3}{2} + 3\hat{a}^2 u^2) + \frac{1}{2}\sigma^2\hat{a}(3 + 4u)u^2 - u^{-3/2}\sqrt{1 + 3\hat{a}\sigma u^2 + \frac{13}{4}\sigma^2 u^3 + \frac{3}{2}\hat{a}\sigma^3 u^5 + (\frac{9}{4}\hat{a}^2 u^7 - 2u^6)\sigma^4}}{\hat{a}^2 - u^{-3} + 3\sigma(\hat{a}^3 u^2 + \hat{a}) + \sigma^2[1 + \hat{a}^2(2u + 3)u^2]}, \quad (22)$$

TABLE I. Characterization of the last stable orbit (LSO) of a spinning particle on circular equatorial orbits of a Kerr background under the MPEQs and the TUL-SSC, Eqs. (1) and (8). The columns report, for each value of $(\hat{a}, \sigma)$ considered, the dimensionless radius of the LSO, $\hat{r}_{\text{LSO}}$, and the corresponding dimensionless orbital frequency, $\hat{\Omega}_{\text{LSO}}$, obtained from Eq. (22).

	$\hat{r}_{\text{LSO}}$			$\hat{\Omega}_{\text{LSO}}$		
$\hat{a}$						
σ	-0.9	0.0	$+0.9$	-0.9	0.0	$+0.9$
$+0.9$	6.606	4.083	1.663	5.572e-02	1.049e-01	3.123e-01
$+0.7$	7.209	4.603	1.755	5.030e-02	9.178e-02	2.938e-01
$+0.5$	7.710	5.063	1.873	4.649e-02	8.243e-02	2.748e-01
$+0.3$	8.147	5.470	2.025	4.357e-02	7.553e-02	2.552e-01
$+0.1$	8.536	5.833	2.216	4.126e-02	7.024e-02	2.350e-01
0.0	8.717	6.000	2.321	4.026e-02	6.804e-02	2.254e-01
-0.1	8.890	6.160	2.429	3.935e-02	6.606e-02	2.165e-01
-0.3	9.216	6.457	2.644	3.774e-02	6.267e-02	2.009e-01
-0.5	9.517	6.729	2.841	3.637e-02	5.988e-02	1.891e-01
-0.7	9.799	6.981	3.011	3.517e-02	5.751e-02	1.808e-01
-0.9	10.062	7.214	3.147	3.412e-02	5.551e-02	1.758e-01

where $u \equiv 1/\hat{r} = M/r$. We use here the minus sign in the $\mp$ case distinction in Eq. (12) of [77] because we define $-1 \le \hat{a} \le 1$ (thus a case distinction is not needed). In the $\sigma \to 0$ limit, this equation reduces to the usual Kepler constraint for a nonspinning particle on Kerr background, $\hat{\Omega} = 1/(\hat{a} + \hat{r}^{3/2})$. Also, when working at linear order in σ, it coincides with the PN expression given by Tanaka *et al.* [51], see Eq. (33) below.

The dimensionless orbital frequency $\hat{\Omega}^{\text{Num}}$ obtained from direct numerical integration of the EoM, Eqs. (1) and (8), is found to agree with the analytical expression Eq. (22) within a fractional difference of 10^{-4} or smaller. We take this as a reliable cross check of the numerical implementation of the dynamics. As a consequence, in the following we will just use Eq. (22) above whenever showing results as a function of the PN-ordering parameter $x \equiv \hat{\Omega}^{2/3}$.

III. TEUKOLSKY FORMALISM IN THE TIME-DOMAIN

In this section we review our approach to solve the TE in the time domain by means of the Teukode (see [60–62] for

further details). We discuss a strategy of computing the source term of the TE for a pole-dipole particle. We spare a detailed repetition of the description of the Teukode, only mentioning that it was validated for a nonspinning particle by reproducing several previous results [78–85].

A. (2 + 1) approach and HH-coordinates

Our approach to solving the gravitational TE makes use of hyperboloidal, horizon penetrating "HH-coordinates" $\{\tau, \rho, \theta, \varphi\}$, see [79,86–90] for general ideas and [61,91] for explicit formulas. The HH-coordinates smoothly reach future null infinity $\mathcal{J}^+$ ("scri"), at ρ_S, and penetrate the horizon at ρ_+, which makes them favorable for numerical computations in two aspects: (i) the domain $[\rho_+, \rho_S]$ is causally closed with vanishing radial coordinate light speeds at the boundaries (thus no numerical boundary conditions have to be imposed), and (ii) ρ_+ and $\mathcal{J}^+$ constitute the two most interesting points for GW-extraction. Since these points are part of the computational domain, we avoid the additional uncertainties of extrapolation procedures. As pointed out in [60,61], the application of these coordinates to the TE has to go hand in hand with a change of the underlying tetrad for the resulting equation to be regular at the horizon and at $\mathcal{J}^+$. A rotation of the tetrad is equivalent to a rescaling of the field $\Psi \to \psi$, see [61] for the explicit rescaling implied by switching from the Kinnersley-tetrad to the Campanelli-tetrad [92], which is used here. The azimuthal coordinate φ is the one from the ingoing-Kerr coordinate system and thus adopted to the axisymmetry of the Kerr spacetime, i.e. $\partial_\varphi = \partial_\phi$, where ϕ is the standard BL-coordinate. Consequently, a decomposition into Fourier m-modes, $\psi = \sum_m \psi_m e^{im\varphi}$, results in components ψ_m of the full solution that decouple upon evolution and can be treated separately. In practice, rederiving the TE in the tetrad of [92] with components specified in the HH-coordinate system and separating the azimuthal dependence, we obtain a reformulated $(2 + 1)$-TE of the form

$$C_{\tau\tau}\partial_{\tau\tau}\psi_m + C_{\tau\rho}\partial_{\tau\rho}\psi_m + C_{\rho\rho}\partial_{\rho\rho}\psi_m + C_{\theta\theta}\partial_{\theta\theta}\psi_m$$
$$+ C_\tau\partial_\tau\psi_m + C_\theta\partial_\theta\psi_m + C_\rho\partial_\rho\psi_m + C_0\psi_m = S_s, \quad (23)$$

with coefficients $C(\rho, \theta; m, s)$ depending on the background coordinates, the spin weight s, and the azimuthal mode-index m. Below, the index m in the complex variable ψ_m will be suppressed for brevity.

B. The source term

The TE, Eq. (23), contains the source term S_s, which encodes the specific form of the matter perturbation that shall be treated. For the gravitational cases the source terms are given by

$$S_{-2} = 8\pi\Sigma(r - ia\cos\theta)^4 T_4, \quad (24)$$

$$S_{+2} = 8\pi\Sigma T_0. \quad (25)$$

The tetrad scalars T_4, T_0 are built from the stress-energy tensor of the perturbation $T^{\mu\nu}$ and from the legs l^μ, n^μ, m^μ of the tetrad, which was used for the derivation of Eq. (23). Schematically, T_4, and similarly T_0, is computed as

$$T_4 = \mathcal{D}_1(T^{\mu\nu}n_\mu n_\nu) + \mathcal{D}_2(T^{\mu\nu}m_\mu m_\nu) + \mathcal{D}_3(T^{\mu\nu}n_\mu m_\nu),$$
$$(26)$$

where the $\mathcal{D}_i$ are certain sums of all kinds of 1st and 2nd coordinate-derivative operators and of nonderivative algebraic factors (see [4] for details).

To be consistent with our dynamics, the model for the stress-energy tensor of a spinning particle must be Mathisson's "gravitational skeleton" in the pole-dipole approximation

$$\sqrt{-g}T^{\mu\nu} = \int d\lambda \{ t^{\mu\nu}(\lambda)\delta^4(x^\mu - X^\mu(\lambda))$$
$$- \nabla_\alpha[t^{\mu\nu\alpha}(\lambda)\delta^4(x^\mu - X^\mu(\lambda))] \}, \quad (27)$$

where $x^\mu = \{\tau, x^i\}$ are some coordinates (in our case the HH-coordinates), λ is the proper time, $X^\mu(\lambda)$ is the world line of the reference point inside the modeled body, $t^{\mu\nu} = v^{(\mu}p^{\nu)}$ is the monopole moment and $t^{\mu\nu\alpha} = S^{\alpha(\mu}v^{\nu)}$ is the dipole moment. Transforming the integral via $d\lambda \to dX^0/(\frac{d}{d\lambda}X^0(\lambda))$ and exploiting the defining properties of a δ-distribution, we obtain the ready-to-use expression (cf. Eqs. (2.14) and (2.16) of [66])

$$T^{\mu\nu}(\tau, x^i) = \frac{1}{\sqrt{-g}} \left\{ \frac{v^{(\mu}p^{\nu)}}{v^t}\delta^3 - \nabla_\alpha\left(\frac{S^{\alpha(\mu}v^{\nu)}}{v^t}\delta^3\right) \right\}, \quad (28)$$

where δ^3 abbreviates $\delta^3(x^i - X^i(\tau))$. In Eq. (28) the dynamical quantities, which are obtained from solving the MPEQs, are depending on the background-coordinate-time, i.e. $X^i(\tau)$, $v^\mu(\tau)$, $p^\mu(\tau)$, $S^{\mu\nu}(\tau)$, but not on the spatial coordinates. The factor $\sqrt{-g}$ and the Christoffel symbols, which enter through the covariant derivative in Eq. (27), are functions of the background and not coordinate time-dependent, at least in time-symmetry adapted coordinates like the HH- or the BL-coordinates. Since the TE source term is computed through Eq. (26) from all kinds of $(\tau, \rho, \theta, \varphi)$-derivatives of $T^{\mu\nu}$, a consistent handling of these dependencies is important.

Unfortunately, the explained "choices" for the dependencies are not unique. The appearance of δ-distributions without any integrals in Eq. (28) creates room for ambiguity. If Eq. (28) was under an integral $\int dx^i(...)$, there would be no doubt that we were free to interchange field and source points, $x^i \leftrightarrow X^i(\tau)$, by virtue of the δ-distributions. But the integral is missing so that we have to consider the δ-distributions as usual functions that only

approximate the distributions in some limit. Therefore, we decide to avoid, (i) interchanging of x^i and X^i at will, and (ii) shifting derivatives that hit the δ-function to the remaining integrand by virtue of $\int dx f(x) \partial_x \delta(x-y) = -\int dx \delta(x-y) \partial_x f(x)$. While these choices are certainly the most reasonable in our opinion, one could still argue that the δ-functions act as if there was an integral. In particular, we mention that Ref. [66] explicitly uses the Christoffel symbols at $X^i(t)$ (working with BL-time t), thus making them t-dependent instead of x^i-dependent. In principle, this leads to slight differences compared to our choice when evaluating the TE-source term. However, a good approximation of the δ-distribution means that $\delta(x^i) \neq 0$ only if $x^i \approx X^i(t)$, which, after all, means the whole discussion becomes irrelevant at high enough resolutions, at least with respect to the numerical outcome.

Let us proceed by discussing briefly the actual implementation of the source term. Since the different derivative terms in Eq. (26) turn out to be of large algebraic complexity, it is advisable to wrap single smaller parts into auxiliary quantities. For instance, one starts by separating the part that in the case of $S^{\mu\nu} = 0$ reduces to the nonspinning particle energy-momentum tensor multiplied by $\sqrt{-g}$, $\tilde{T}^{\mu\nu}_{\mathrm{NS}} = v^{(\mu} p^{\nu)} \delta^3 / v^t$, from the explicitly $S^{\mu\nu}$-dependent part $\tilde{T}^{\mu\nu}_{\mathrm{SP}}$, which reads

$$\sqrt{-g} T^{\mu\nu} = \tilde{T}^{\mu\nu}_{\mathrm{NS}} + \tilde{T}^{\mu\nu}_{\mathrm{SP}}. \tag{29}$$

Note though that the rewriting $\tilde{T}^{\mu\nu}_{\mathrm{NS}} = \mu v^\mu v^\nu \delta^3 / v^t$, which we used in [61], does not hold anymore because we have $p^\mu \neq \mu v^\mu$ if $S^{\mu\nu} \neq 0$. We further separate the explicitly spin-dependent part into pieces, according to

$$\tilde{T}^{\mu\nu}_{\mathrm{SP}} = Q^{\mu\nu}_A + Q^{\mu\nu}_B + Q^{\mu\nu}_C + Q^{\mu\nu}_D,$$
$$Q^{\mu\nu}_A := \partial_\tau (S^{0(\mu} V^{\nu)} \delta^3),$$
$$Q^{\mu\nu}_B := S^{i(\mu} V^{\nu)} \partial_i \delta^3,$$
$$Q^{\mu\nu}_C := S^{\rho\mu} V^\sigma \Gamma^\nu_{\rho\sigma} \delta^3,$$
$$Q^{\mu\nu}_D := S^{\rho\nu} V^\sigma \Gamma^\mu_{\rho\sigma} \delta^3, \tag{30}$$

where we have introduced the coordinate velocities $V^\mu = v^\mu / v^\tau$ and exploited the antisymmetry of $S^{\mu\nu}$. In the code, the derivatives of $\tilde{T}^{\mu\nu}_{\mathrm{SP}}$ are then computed as sums of derivatives of the $Q^{\mu\nu}_X$. Notably, $Q^{\mu\nu}_A$ and $Q^{\mu\nu}_B$ already contain $\partial\delta$-terms, which means that we will end up with a source term that includes third derivatives of the δ-functions, i.e. $\partial\partial\partial\delta$-terms. It remains to compute derivatives of the tetrad legs and, finally, to shuffle all the pieces together.

At last, we emphasize that in the Teukode the whole computation outlined above is performed in the HH-coordinate system. This is not necessarily to be expected since T_0 and T_4 are tetrad scalars and thus coordinate invariants, but it turns out that the δ-function treatment is simplified if the source is treated within the same

coordinates as the rest of the equation, see Sec. III. 2 in [61]. This means, after solving the MPEQs in Boyer-Lindquist coordinates, we have to transform $\{X^\mu, v^\mu, p^\mu, S^{\mu\nu}\}$ before feeding them to the code.

C. Numerical approximation of δ-functions

The performance of different numerical approximations of a δ-distribution, and of its derivatives in r and θ, was discussed already in [61]. However, when the particle is spinning the presence of third derivatives of δ-functions in the source term obliges us to reconsider what is the best option. Inspecting the recent literature, one finds that a δ-like source can be implemented essentially in two ways: (i) a few-point (discrete) approximation, developed in [83,93,94], and (ii) a simpler, analytical approximation by a (narrow) Gaussian function. Within our numerical infrastructure, the two representations for the δ-function were extensively compared in [61]. It was found that the few-point representation is superior to the extended representation for CEOs. In that case we were able to reproduce the values for energy fluxes emitted by a nonspinning particle as computed by S. Hughes by means of an improved version of the frequency-domain code used in [83,84,95] (see Appendix A of [96]) within 0.01% at a resolution of $N_\rho \times N_\theta = 2400 \times 200$ points. In general, however, for noncircular motion the Gaussian approximation of the δ-function turned out to be the better option as it caused less numerical noise in the simulation.

In the present study of CEOs we use the narrow-Gaussian model because, (i) it will be our standard choice when deviating from circular motion in the future, and (ii) the prescriptions for building a few-point representation of third derivatives of a delta-function have not been derived in [83] (though following the same ideas they can be in principle). This approximation implies a slight loss of accuracy compared to our results for a nonspinning particle [61]. The fractional accuracy we obtain is about 0.2% in the dominant $m = 2$ mode (see below), which is sufficient to prove the consistency between the PN and the numerical fluxes at large orbital radii.

IV. RESULTS: COMPARING NUMERICAL AND POST-NEWTONIAN FLUXES FOR CIRCULAR ORBITS

In this section we present our new numerical computation of the GW energy fluxes emitted by a spinning particle on a CEO about a Kerr black hole. We discuss the total flux to infinity [97], which is approximated here as the sum over the three dominant $m = 1, 2, 3$ multipoles, with all corresponding ℓ-contributions included, and compare it with the 2.5PN prediction. We see that the result of the numerical computation and the analytical PN prediction are consistent (up to the 0.2% level) for large orbital radii, i.e. when $x \equiv \hat{\Omega}^{2/3} \to 0$. A detailed multipolar analysis is presented in Appendix A.

We mention the possibly obvious fact that our results hold analogously for angular momentum fluxes. For circular orbits the energy fluxes and the angular momentum fluxes are trivially connected via $\frac{dJ}{dt} = \frac{m}{\omega}\frac{dE}{dt}$, (see Eq. (4.13) in [98]). Here, the orbital frequency of the particle, Ω, determines the waveform's frequency $\omega = m\Omega$.

A. Numerical fluxes and their accuracy

In this section we will give an estimate of the accuracy of our energy flux computations on the basis of *non*spinning particle experiments, which can be quantitatively compared with existing literature results. More precisely, we compute the fluxes of a *non*spinning particle on a CEO, with the same numerical setup that will be used for a spinning particle, i.e. using the Gaussian approximation of the δ, and then we compare with the extremely accurate target solution computed by S. Hughes in the frequency domain [83,84,95,96].

In [61], we have performed the same comparison and found a $\sim 0.01\%$ agreement at resolutions $N_\rho \times N_\theta = 2400 \times 200$. However, this remarkable accuracy relies on the usage of the few-point delta-approximation of [83]. The Gaussian δ-approximation, which we use here, is expected to entail a loss of accuracy. To compensate the loss of accuracy, we increase the resolution in this study to $N_\rho \times N_\theta = 4800 \times 400$ points. As shown below, this is enough to reach satisfactory accuracy for $\hat{r} \leq 20$. When studying orbits at $\hat{r} = 30$, the accuracy drops due to the loss of resolution near the compactification boundary in the hyperboloidal coordinate system. Therefore, at $\hat{r} = 30$ we employ extraordinary resolutions of $N_\rho \times N_\theta = 6000 \times 500$.

Before going into detail on the accuracy, we discuss how the energy fluxes can be computed from our master variable ψ. At future null infinity, $\rho = \rho_S$, our master variable satisfies $\psi(\tau, \rho_S, \theta, \varphi) = r\Psi_4(\tau, \theta, \varphi)$. Therefore, we can compute the multipolar energy fluxes to infinity directly from ψ, which for the multipolar decomposition reads

$$F_{\ell m} = \frac{2}{16\pi}|r\dot{h}_{\ell m}|^2 = \frac{2}{4\pi\omega^2}|\psi_{\ell m}|^2, \qquad (31)$$

where $r\dot{h} = 2\int \psi dt'$. The multipolar energy flux $F_{\ell m}$ is here defined to include both the $+m$ and $-m$ contributions, which implies the factor 2 in Eq. (31), cf. Eq. (2) of [63]. Note that the ℓm-subscript refers to a multipolar decomposition that can be done either with respect to the spin-weighted spherical harmonics $Y_{s\ell m}$ or the spin-weighted spheroidal harmonics $S_{s\ell m}$, see Appendix A 1 for a short description of these functions. Notably, the reference data for $\sigma = 0.0$ includes the multipolar fluxes with respect to both the $Y_{2\ell m}$ and the $S_{-2\ell m}$ bases.

Let us proceed by comparing our numerical results and the target solution of Hughes for $\sigma = 0.0$. As a general benchmark, we find an agreement of $\sim 0.2\%$ in the full ℓ-summed flux of a $m = 2$ simulation for all tested background spins $\hat{a} \in \{0, \pm 0.9\}$, and at all radii, $\hat{r} = (4, 5, 6, 7, 8, 10,$

12, 15, 20, 30). We find approximately the same accuracy in the dominant multipolar fluxes. For example, at $\hat{r} = 20$ for $\hat{a} = \pm 0.9$ the multipolar 22-flux, either with respect to Y_{-222} or to S_{-222}, exhibits again a $\sim 0.2\%$ agreement with the reference solution. For the subdominant modes the accuracy decreases slightly because they are much smaller in absolute magnitude; e.g., for both the Y_{-232}-flux and the S_{-232}-flux we find a $\sim 0.5\%$ agreement in the $\hat{r} = 20$, $\hat{a} = \pm 0.9$ test cases. In conclusion, the estimated $\lesssim 0.2$–0.5%-level of accuracy for $\sigma = 0.0$ is surely enough to prove consistency with the corresponding PN expressions, though nonzero values of the spin, $\sigma \neq 0$, are expected to slightly increase the amount of noise in our simulations. To get an immediate impression of the accuracy of our multipolar fluxes, we have added the nonspinning $\sigma = 0.0$ results of [84] to our plots of the multipolar fluxes over σ, Fig. 2. The $\sigma = 0.0$ data points are highlighted by short horizontal gray lines, which should be cut by the smooth connection of our $\sigma \neq 0$ data points.

It is now necessary to point out a further practical detail regarding our flux computations. The two relations in Eq. (31), i.e. the computation in terms of $\dot{h}$ and in terms of ψ respectively, are analytically equivalent, but in practice we find a crucial numerical difference at large radii. At small radii, we find that both computations are numerically indifferent, as expected. For example, for $\hat{a} = -0.9$ at $\hat{r} = 5$ we find an agreement between both computations of $\sim 0.00001\%$, independently from the considered value of σ. At larger radii the agreement between the two ways to compute the fluxes gets progressively worse; for example, at $\hat{r} = 20$ it amounts to $\sim 0.01\%$, which is still equivalent for our purpose from a practical point of view. But, at $\hat{r} = 30$ it can make a significant difference whether the fluxes are computed from ψ directly or from $\dot{h}$ after integration. For example, doing a test at $\hat{r} = 30$ with $\hat{a} = 0.9$ and $\sigma = 0.0$, the computation using $\dot{h}$ works reliably—we find a deviation in the full $m = 2$ flux (including all ℓ contributions) from the target solution of only $\sim 0.1\%$. On the contrary, the computation of fluxes directly from ψ is more biased by numerical noise—we find, e.g., for the flux in the Y_{21}-mode a deviation of $\sim 1.8\%$ from the target. For $\sigma \neq 0$ the level of noise can be even worse so that we cannot in all cases extract an unambiguous energy flux directly from ψ.

The better accuracy in case of using $\dot{h}$ for the flux computation originates from the cumulative integration: it acts like a filter for the numerical noise, which is present in all our simulations since we do not employ any numerical dissipation. At small radii, $\hat{r} \leq 20$ the absolute values of our fields are so large that the noise is at a negligible level. At large radii, $\hat{r} > 20$, however, the amplitude of the fields becomes so small that the numerical noise can spoil the accuracy of our computations. In summary, we are able to extract energy fluxes at large radii, $\hat{r} > 20$, in a robust way when using a numerical integration of ψ to obtain $\dot{h}$. Unfortunately, in the data sets that we had compiled for this study these integrations were only performed for the

$Y_{-2\ell m}$-fluxes, whereas the $S_{-2\ell m}$-fluxes were computed using ψ directly and are thus only stated up to $\hat{r} = 20$. In the future, another possibility is to use numerical dissipation, which is implemented though not used for this study because our initial tests at small radii did not suggest that it might be needed.

Finally, as another interesting side remark, we mention that the fluxes in the (2,2),(2,1),(3,3)-modes are practically equal when doing the multipolar decomposition either with respect to $Y_{-2\ell m}$ or to $S_{-2\ell m}$. For example, for $\hat{a} = \pm 0.9$ at $\hat{r} = 20$ the Y_{-222}-flux and the S_{-222}-flux differ by only $\sim 0.01\%$. Similarly, at this configuration the Y_{-221}-flux and the S_{-221}-flux, and the Y_{-233}-flux and the S_{-233}, differ by $\sim 0.02\%$. This agreement is sustained, to large extent, even at strong-field radii, where the frequencies—and thus the differences between the Y-functions and the S-functions— are larger. For example, at $\hat{r} = 5$ the Y_{-222}-flux and the S_{-222} flux differ by $\sim 0.2\%$ for $\hat{a} = +0.9$, and by $\sim 0.5\%$ for $\hat{a} = -0.9$. In summary, for these modes any discussion held in terms of a $S_{-2\ell m}$-decomposition holds to large extent as well for a $Y_{-2\ell m}$-decomposition. On the contrary, the fluxes in the (3,2)-mode are drastically different in the two basis-systems. For example, at $\hat{r} = 20$ for $\sigma = 0.0$ and $\hat{a} = 0.9$ we find deviations of $\sim 60\%$ (!).

B. Analytics: Post-Newtonian energy fluxes

Tanaka *et al.* [51] computed, long ago, in post-Newtonian theory, the GW energy fluxes emitted by a spinning particle on a CEO about a Kerr black hole. Their results hold at 2.5PN-order, and are linear in the particle spin, i.e. including only leading-order (LO) spin contributions. The respective formulas are expressed using the dimensionless spin magnitude (called $\hat{s}$ in [51]). The main result of [51] is the total energy flux to infinity, which reads, in terms of $u \equiv M/r$, where r is the BL-coordinate radius,

$$F = \frac{32}{5}\nu^2 u^5 \left\{ 1 - \frac{1247}{336}u + \left(4\pi - \frac{73}{12}\hat{a} - \frac{25}{4}\sigma\right)u^{3/2} \right.$$
$$+ \left(-\frac{44711}{9072} + \frac{33}{16}\hat{a}^2 + \frac{71}{8}\hat{a}\sigma\right)u^2$$
$$\left. + \left(-\frac{8191}{672}\pi + \frac{3749}{336}\hat{a} + \frac{2403}{112}\sigma\right)u^{5/2}\right\}, \quad (32)$$

where $\nu \equiv \mu/M$ is the mass ratio. Note that in [51] the notation $v^2 = M/r$ was used, which we will *not* follow here

in view of the fact that M/r is not the orbital velocity (except for $\hat{a} = \sigma = 0$). To drive comparisons with numerical data, as well as with other PN results, one has to recast the above expression into a formulation in terms of the gauge-invariant standard PN-ordering parameter $x \equiv \hat{\Omega}^{2/3}$. Note that, for nonzero values of $(\hat{a}, \sigma)$, one has $x \neq u$, i.e $\hat{\Omega} \neq u^{3/2}$. To rewrite Eq. (32), first in terms of $\hat{\Omega}$ and subsequently in terms of x, one can PN-expand the analytic expression for the frequency, Eq. (22), which yields

$$\hat{\Omega} = u^{3/2}\left[1 - \left(\frac{3}{2}\sigma + \hat{a}\right)u^{3/2} + \frac{3}{2}\hat{a}\sigma u^2 + O(u^3)\right], \quad (33)$$

see Eq. (5.18) in [51]. We invert this equation, insert it into Eq. (32), and, adopting the notation

$$F(x, \hat{a}, \sigma) \equiv F_N(x)\hat{F}(x, \hat{a}, \sigma), \quad (34)$$

$$F_N(x) \equiv \frac{32}{5}\nu^2 x^5, \quad (35)$$

we obtain

$$\hat{F}(x, \hat{a}, \sigma) \equiv 1 - \frac{1247}{336}x + \left(4\pi - \frac{11}{4}\hat{a} - \frac{5}{4}\sigma\right)x^{3/2}$$
$$+ \left(-\frac{44711}{9072} + \frac{33}{16}\hat{a}^2 + \frac{31}{8}\hat{a}\sigma\right)x^2$$
$$+ \left(-\frac{8191}{672}\pi - \frac{59}{16}\hat{a} - \frac{13}{16}\sigma\right)x^{5/2}. \quad (36)$$

Note the minus sign in front of $(59/16)\hat{a}$, which corrects the wrong plus sign in Eq. (5.19) of Tanaka *et al.* [51]. It is also pleasing to note that Eq. (36) agrees, up to the expected PN-order, with the respective PN-prediction for the comparable mass case, Eq. (4.9) of [57], when restricted to the test-particle limit $\nu \to 0$.

For completeness, we also rewrite the multipolarly decomposed fluxes, which were provided by Tanaka *et al.* in terms of u, in terms of x. It is important to mention that the multipolar decomposition is performed here with respect to the spin-weighted spheroidal harmonics, $S_{s\ell m}$. Each multipolar flux can be separated into its LO contribution and higher-order corrections, $F_{S_{\ell m}} \equiv F_{\ell m}^{LO}\hat{F}_{S_{\ell m}}$. In this way we obtain

$$\hat{F}_{S_{22}} = 1 - \frac{107}{21}x + \left(4\pi - \frac{8}{3}\hat{a} - \frac{4}{3}\sigma\right)x^{3/2} + \left(\frac{4784}{1323} + 2\hat{a}^2 + 4\hat{a}\sigma\right)x^2 + \left(-\frac{428}{21}\pi + \frac{52}{27}\hat{a} + \frac{208}{63}\sigma\right)x^{5/2}, \quad (37)$$

$$\hat{F}_{S_{21}} = 1 + 3(\sigma - \hat{a})x^{1/2} + \left(-\frac{17}{14} + \frac{9}{4}\hat{a}^2 - \frac{9}{2}\hat{a}\sigma\right)x + \left(2\pi + \frac{215}{252}\hat{a} - \frac{367}{28}\sigma\right)x^{3/2}, \quad (38)$$

$$\hat{F}_{S_{33}} = 1 - 8x + (6\pi - 3\sigma - 4\hat{a})x^{3/2}, \quad (39)$$

$$\hat{F}_{S_{32}} = 1 + \left(4\sigma - \frac{8}{3}\hat{a}\right)x^{1/2}, \tag{40}$$

$$\hat{F}_{S_{31}} = 1 - \frac{16}{3}x + \left(2\pi + 5\sigma - \frac{100}{9}\hat{a}\right)x^{3/2}. \tag{41}$$

In the main body of this paper we focus on the total flux, but in Appendix A also these formulas are compared (and found to be consistent) with the corresponding numerical results.

C. Comparing numerical and PN total GW fluxes

Now, we compare and contrast the outcome of our numerical computation of the full energy flux with the 2.5PN information, as given by Eq. (36). This comparison is only meaningful in a finite region of parameter space because our numerical results are inaccurate for too large radii ($r > 30M$) while the PN prediction is not expected to be reasonable for too small radii (say, rather arbitrarily, $r \lesssim 15M$). At any rate, we have to settle with observing the expected trend when traversing the region of common validity $r \in [15M, 30M]$ but are not able to cross-check numerics with analytics at an arbitrary accuracy in the region $r \to \infty$.

The main result of our study is the unambiguous trend of the total energy flux, approximated as the sum over the $m = 1, 2, 3$ contributions in our numerical data, against the 2.5PN prediction Eq. (35), as highlighted in Fig. 1. To our knowledge, it is the first time that this comparison is done. Figure 1 shows the numerical fluxes together with the 2.5PN predictions for several values of $\hat{a}$ and σ. The $\sigma = 0$ data (blue, circles) in Fig. 1 are not produced with our code, but were computed by S. Hughes at extreme accuracy in the frequency domain and were kindly made available to us for completing the comparison here. To be consistent with our $\sigma \neq 0$ data, we compute the $\sigma = 0.0$ total flux by summing over multipoles $m = 1, 2, 3$ and $\ell = 1, ..8$. Note that we make the choice to stay consistently at 2.5PN though higher-order information up to 22PN for Schwarzschild [99] and 20PN for Kerr [100] are available in the literature for a nonspinning particle.

Inspecting Fig. 1, one can draw several conclusions from our numerical computations. First, if $\sigma < 0$, the GW flux is increased with respect to the $\sigma = 0$ case, while, if $\sigma > 0$, it is decreased. This holds independently of the background spin $\hat{a}$, i.e. for all three panels of Fig. 1. Second, one sees that the prediction of the approximate PN series is qualitatively consistent with the numerical data because there is a clear trend of numerics (solid lines) toward analytics (dashed lines) as $x \to 0$; one sees that the disagreement between PN and numerical data progressively decreases as x becomes smaller. In particular, the spin-dependence is captured correctly in the numerics, i.e. though evidently all the
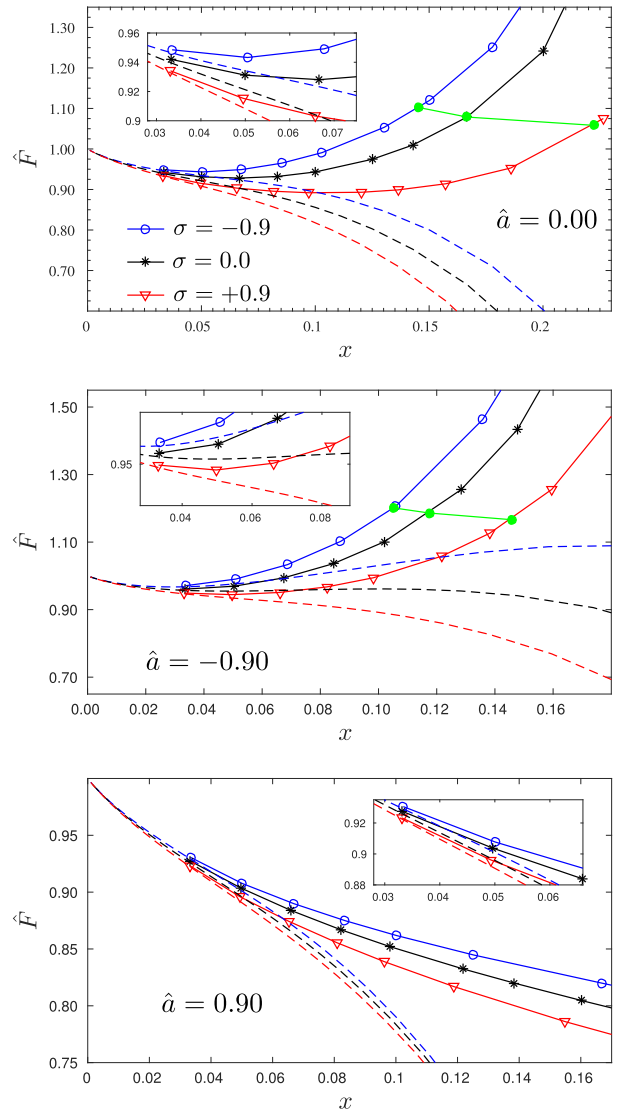

FIG. 1. Comparison of numerical (solid) and analytical PN (dashed) total energy fluxes over $x = \hat{\Omega}^{2/3}$. We consider three values of the background spin, $\hat{a} = 0.0$ (top panel), $\hat{a} = -0.9$ (middle panel), and $\hat{a} = +0.9$ (bottom panel). For each value of $\hat{a}$, we plot the fluxes for a spinning particle with spins $\sigma = -0.9$ (blue, circles), $\sigma = 0.0$ (black, stars) with data computed by Hughes [83,84,95,96], see text, and $\sigma = +0.9$ (red, triangles) over x. The numerical fluxes are obtained summing up the modes with $m = 1, 2, 3$; the PN fluxes are given by Eq. (36), which sums up only the modes considered in [51]. The green filled circles mark the interpolated fluxes at the locations of the LSO, cf. Table I. At low orbital frequencies $\hat{\Omega} \to 0$, or equivalently $x \to 0$ and $\hat{r} \to \infty$, the numerics are consistent with the PN-prediction, reaching in all cases a fractional difference $\leq 0.5\%$ at our outermost data point $\hat{r} = 30$, see also Tables II–IV.

normalized fluxes converge toward ~ 1, and thus toward one another, the offset between the $\sigma = 0.0$ and the $\sigma \neq 0$ lines is consistent in the numerics and in the analytics, as highlighted in the small insets in Fig. 1. Quantitatively, the visual comparison is supported by the data shown in Tables II–IV in Appendix B. For example, focusing first on the $\hat{a} = 0$ case, one sees that at $\hat{r} = 20$, i.e. $x \approx 0.05$, the relative deviations amount to 1% for $\sigma = -0.9$ and to 0.7% for $\sigma = 0.9$. At $\hat{r} = 30$, i.e. $x \approx 0.033$, they have decreased to 0.23% for $\sigma = -0.9$ and 0.14% for $\sigma = 0.9$. This is almost reaching the level of accuracy, $\sim 0.2\%$ of our numerical results, as estimated in Sec. IV A. A similar consistency is found when $\hat{a} \neq 0$. For $\hat{a} = -0.9$, at $\hat{r} = 30$ the agreement has reached 0.33% for $\sigma = -0.9$ and 0.25% for $\sigma = 0.9$. For $\hat{a} = +0.90$, the fractional difference at $\hat{r} = 30$ between the numerical and the PN prediction is 0.16% for $\sigma = -0.9$ and 0.08% for $\sigma = 0.9$. These results mutually confirm the 2.5PN predictions as well as our numerical computations.

Finally, we mention that the consistency check for $x \to 0$ can be repeated in the same way for the multipolar fluxes, Eqs. (37)–(41), instead of the total flux. Without illustration, we have included the corresponding data in Table II–IV. The trend is again unambiguous, though a bit worse than in the total flux, especially if $(\ell, m) \neq (2, 2)$; likely, simply because the subdominant modes themselves are, (i) at 2.5PN known with too few terms after the LO-contribution; e.g., the formula for the flux in the (3,2)-mode, Eq. (40), only includes one term beyond LO, and (ii) smaller in absolute value and, therefore, relatively more affected by the numerical noise. For more details, see the multipolar analysis of the fluxes with respect to the spin σ at a fixed radius in Appendix A (notably, discussed there in a one-to-one comparison with the formulas given by [51], i.e. without the change of variables $u \to x$).

V. CONCLUSIONS

In this paper we have presented a new computation of the gravitational wave fluxes emitted by a spinning particle on circular equatorial orbits of a Kerr black hole. This is done, for the first time, by solving the Teukolsky equation in the time domain, using the Teukode of [61,62], for a pole-dipole particle source term that is built according to the Mathisson-Papapetrou-equations under the Tulczyjew-spin-supplementary condition. We investigated three values of the background spins, $\hat{a} = 0$ and $\hat{a} = \pm 0.9$, and ten values of the particle spin $\sigma/\nu \in \pm\{0.1, 0.3, 0.5, 0.7, 0.9\}$. We stress that there is no technical obstruction to obtain data at even higher rates for the spins.

About 20 years ago Tanaka *et al.* [51] computed the GW energy fluxes for the considered test-particle setup

at the 2.5PN order. Recently, Marsat *et al.* [57] performed the respective comparable-mass PN calculation (see also [52,54,55]), which contains Tanaka *et al.*'s result as a special case in the test-particle limit and extends it by terms up to 4PN. While Tanaka *et al.*'s results were thus analytically confirmed, a detailed numerical check of their accuracy was missing. In this work, for the first time, we proved the consistency between numerical results and the post-Newtonian calculations of the GW fluxes at 2.5PN. More precisely, at our outermost data point, $\hat{r} = 30$, we find a relative disagreement between the total numerical flux, approximated as the sum over $m = 1, 2, 3$ mode contributions, and the 2.5PN result, Eq. (5.19) of [51], at the order of $\leq 0.5\%$ for all considered values of $\hat{a}$ and σ. This mutually confirms the numerically untested 2.5PN prediction and our numerical computations. Moreover, we mention that our results seem to disagree quantitatively with the corresponding numerical results of [44], though we observe a certain qualitative consistency (see Appendix A). We have presented our results in the form of a central plot, Fig. 1, and supported the visual impression quantitatively by data tables, Tables II–IV. Notably, such database is missing from the literature and will provide a valuable orientation for future studies in the same direction. Additionally, the numerical data presented here will serve as a test bed for developing suitably resummed expressions for the PN fluxes—a procedure which was successfully developed for a nonspinning particle and which drastically improved the regime of accuracy of straight PN expressions toward the strong-field regime [63–65]. Thus, our numerical results will have immediate impact in modeling analytically the radiation reaction force for a spinning particle in quasicircular, adiabatic inspiral motion about a rotating BH background, and, in turn, to the effective-one-body model with generic spins.

ACKNOWLEDGMENTS

APPENDIX A: COMPLEMENTARY DISCUSSIONS

In this Appendix we provide some complementary information on the comparison of our numerical results

with the 2.5PN predictions of [51]. First, we perform the analysis multipole by multipole, discussing the cases $\ell m = 22, 21, 33, 32$. This comparison is conducted in a slight alteration with respect to the main body of this paper because here we remain with the variable $u \equiv M/r$ instead of switching to $x \equiv \hat{\Omega}^{2/3}$. Note that this allows the check of the, so to say, raw result of the computations performed in [51]; the switch $u \rightarrow x$, which we used in the main body, is necessary to argue in terms of usual PN parameters, but it amounts to an additional approximation by using the PN expansion of the frequency, Eq. (33), which, in particular, is only linear in the spin. In the second part, we will then repeat the consistency check of the full energy flux in terms of u, complementing the comparison shown in the main body in terms of x.

1. Spin-weighted spheroidal harmonics

While the focus in the main body of the paper is on the full flux, the data in Tables II–IV, and the discussion in this appendix include also comparisons of the separate multipolar contributions. Therefore, we emphasize again that the results of Tanaka et al. [51] on multipolar fluxes, as well as the rewriting of these results in terms of other variables, Eqs (37)–(41), refer to a decomposition with respect to the spin-weighted spheroidal harmonics, $S_{s\ell m}$.

Spin-weighted spheroidal harmonics arise in the traditional separation of the original TE in the frequency domain. The angular part of the resulting ordinary differential equations, Eq. (2.7) in [98], describes an eigenvalue problem for each relevant ω of the solution. The eigenfunctions are what we call $S_{s\ell m}$, with eigenvalue $E_{s\ell m}$. For $\hat{a} = 0$ they reduce to the well-known spin-weighted spherical harmonics (see, e.g., [101]). In the case of circular equatorial orbits ω is fixed, and thus there is a unique set of $S_{s\ell m}$ functions, which forms a complete basis. The analytic formulas of Tanaka et al. are given with respect to a decomposition in terms of the $S_{s\ell m}$-basis. Hence, to make comparisons of the multipolar fluxes we also project our full solution onto modes with respect to the $S_{s\ell m}$-basis. The computation of the $S_{s\ell m}$ is not trivial, but a nice procedure is given in Appendix A of [84], which we adopted here (cf. also [4,102]).

2. Multipolar analysis at fixed radius

Let us recall the 2.5PN results for the multipolar fluxes, Eqs (5.16) of [51]. The stated quantities are the normalized fluxes $\eta_{\ell m} = F_{S_{\ell m}}/(32/5 u^5)$ for $\ell m = \{22, 21, 33, 31, 32, 44, 42\}$, where $F_{S_{\ell m}}$ is the multipolar flux in the $\ell \pm m$-modes, with the definition of the $F_{S_{\ell m}}$ used above, see also Eq. (2) of [63]. It is important to note that the normalization factor is, in general, not the

usual Newtonian flux, $F_{22}^N = (32/5)x^5$. Thus one has to mind the different normalization with respect to that used in the main body of this paper. Concretely, the multipolar 2.5PN-formulas as given by [51] versus u read,

$$\eta_{22}(\hat{a}, \sigma, u) = 1 - \frac{107}{21}u + \left(4\pi - 6\hat{a} - \frac{19}{3}\sigma\right)u^{1.5}$$
$$+ \left(\frac{4784}{1323} + 2\hat{a}^2 + 9\hat{a}\sigma\right)u^2$$
$$+ \left(-\frac{428}{21}\pi + \frac{4216}{189}\hat{a} + \frac{2134}{63}\sigma\right)u^{2.5},$$
(A1)

$$\eta_{21}(\hat{a}, \sigma, u) = \frac{1}{36}u + \left(-\frac{1}{12}\hat{a} + \frac{1}{12}\sigma\right)u^{1.5}$$
$$+ \left(-\frac{17}{504} + \frac{1}{16}\hat{a}^2 - \frac{1}{8}\hat{a}\sigma\right)u^2$$
$$+ \left(\frac{1}{18}\pi - \frac{793}{9072}\hat{a} - \frac{535}{1008}\sigma\right)u^{2.5},$$
(A2)

$$\eta_{33}(\hat{a}, \sigma, u) = \frac{1215}{896}u - \frac{1215}{112}u^2$$
$$+ \left(\frac{3645}{448}\pi - \frac{1215}{112}\hat{a} - \frac{10935}{896}\sigma\right)u^{2.5},$$
(A3)

$$\eta_{32}(\hat{a}, \sigma, u) = \frac{5}{63}u^2 + \left(-\frac{40}{189}\hat{a} + \frac{20}{63}\sigma\right)u^{2.5},$$
(A4)

$$\eta_{31}(\hat{a}, \sigma, u) = \frac{1}{8064}u - \frac{1}{1512}u^2$$
$$+ \left(\frac{1}{4032}\pi - \frac{17}{9072}\hat{a} - \frac{1}{8064}\sigma\right)u^{2.5}.$$
(A5)

Unfortunately, the 31-mode is too weak to be measured accurately in our numerics, especially for orbits in the weak-field, which we rely on for the validation of our data. Also, the 44 and 42 energy fluxes do not contain spin-dependence at 2.5PN. Consequently, we restrict the comparison below to the $\ell m = \{22, 21, 33, 32\}$ modes. For our comparison we find it convenient to further normalize each $\eta_{\ell m}$ to the corresponding LO term. For clarity, reading off the LO terms from Eqs (A1)–(A5) and combining with F_{22}^N, we obtain the following expressions: $\hat{\eta}_{22} = \eta_{22} = F_{22}/(\frac{32}{5}u^5)$, $\hat{\eta}_{21} = F_{21}/(8u^6/45)$, $\hat{\eta}_{33} = F_{33}/(243u^6/28)$, $\hat{\eta}_{32} = F_{32}/(32u^7/63)$, which are all of the form $\sim 1 + \mathcal{O}(u)$.

In Fig. 2 we have collected at a glance our numerical results for the multipolar fluxes $\hat{\eta}_{\ell m}$ and contrasted them
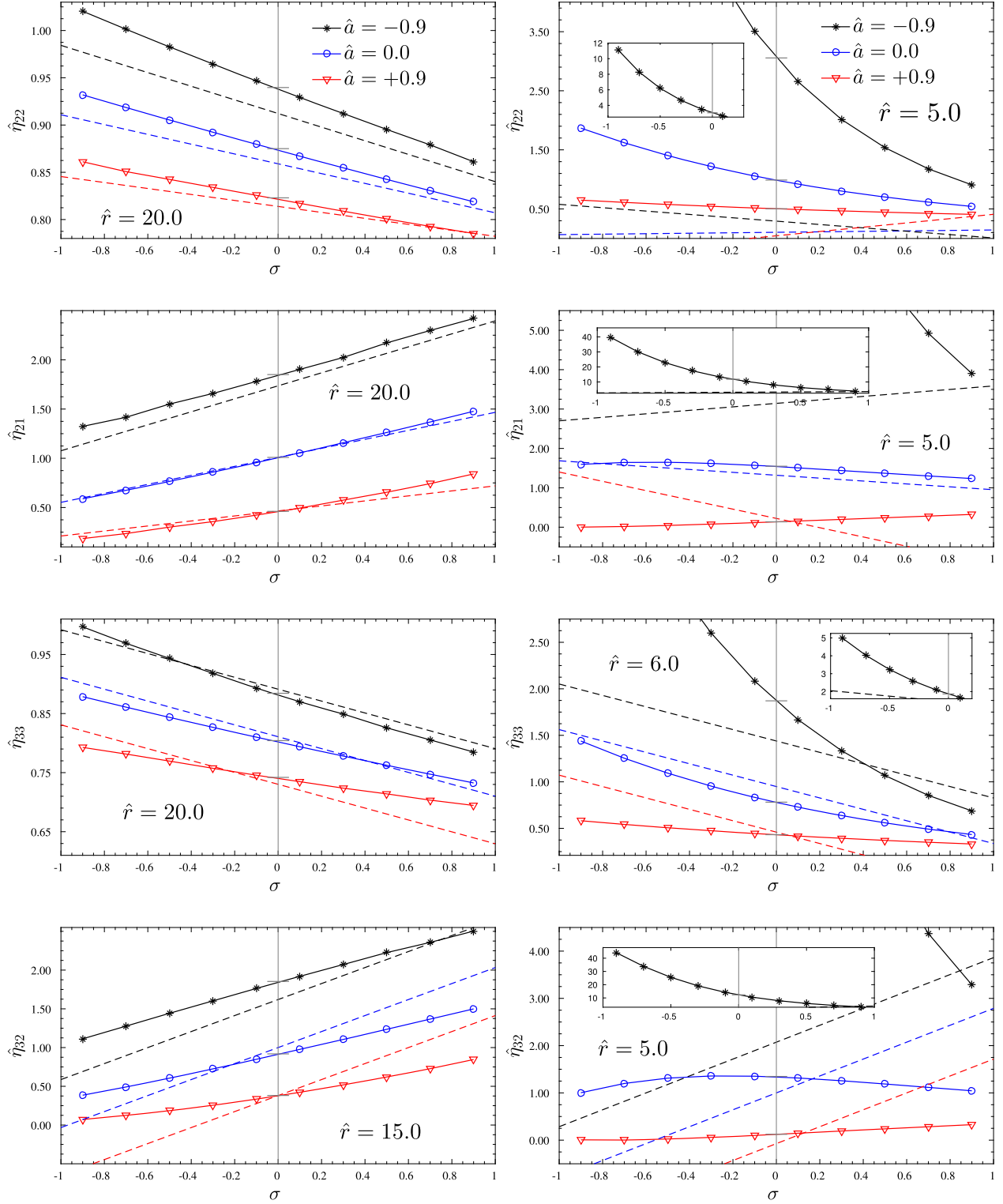
FIG. 2. Dependence of the LO-normalised multipolar fluxes, $\eta\ell m$ on the spin σ, comparing numerical results (solid) with 2.5PN analytical predictions (dashed), at a weak-field orbit (left) and a strong-field orbit (right), for the three background spins $\hat{a} = 0.0$ (blue, circles), $\hat{a} = -0.9$ (black, stars), and $\hat{a} = +0.9$ (red, triangles). The panels show the multipolar energy fluxes in the S_{-222} (top), S_{-221} (top middle), S_{-233} (bottom middle) and S_{-233} (bottom) modes. The small horizontal lines on the $\sigma = 0.0$ axis refer to the results for a nonspinning particle from the frequency-domain data of Hughes [84]. Note, for clarity, that these plots show the $\hat{\eta}_{\ell m}$, as obtained from Eqs. (A1)–(A5) by normalizing with the LO-Newtonian expressions in terms of $u \equiv 1/r$ (e.g., for $\ell m = 22$ with $32/5u^5$), whereas the values stated in Tables II–IV refer to the $\hat{F}_{S_{\ell m}}$ and are thus normalized to the LO-Newtonian expressions in terms of $x \equiv \hat{\Omega}^{2/3}$ (e.g., for $\ell m = 22$ with $32/5x^5$).

with the 2.5PN predictions. To guide the reader through the many panels, note first that the different modes $(\ell, m) \in \{(2, 2), (2, 1), (3, 3), (3, 2)\}$ are arranged in Fig. 2 from top to bottom, where for each mode we have one weak-field (left panels) and one strong-field (right panels) comparison of numericals fluxes with PN predictions. For each comparison we consider the three different background spins $\hat{a} = -0.9$ (black, stars), $\hat{a} = 0.0$ (blue, circles), and $\hat{a} = 0.9$ (red, triangles). The σ data points are computed at $\pm\{0.1, 0.3, 0.5, 0.7, 0.9\}$. To illustrate the smooth connection of our data to the correct $\sigma = 0.0$ values, which are again made available to us at highest accuracy by Hughes [83,84,95,96], we draw short, gray, horizontal lines at the respective $\sigma = 0$ values.

Let us discuss first the weak-field comparison illustrated in the left column of panels. For all four modes, our numerical fluxes (solid lines) are consistent with the 2.5PN predictions (dashed lines), i.e. with the LO-normalized versions of Eqs. (A1)–(A5). Only in the (3,2)-mode the spin-behavior is poorly captured by the analytics, but note that in this case we show the comparison at an orbital separation of $\hat{r} = 15$. At $\hat{r} = 20$ and for $\sigma = -0.9$ the (3,2)-flux was too small in absolute value to be measured reliably. But even at $\hat{r} = 20$ we would not expect a much better agreement because the 2.5PN formula for the (3,2)-mode reaches only one term beyond the leading order. The comparisons between numerics and PN predictions for strong-field orbits are shown in the right column of panels. It is apparent from the plot that there is a clear failure of the PN formulas in the strong-field regime. Especially for $\hat{a} = -0.9$, in which case the LSO is located at $r_{\mathrm{LSO}} \approx 6.6$ for $\sigma = +0.9$ and $r_{\mathrm{LSO}} \approx 10.0$ for $\sigma = -0.9$ the numerical results are completely off the prediction. For $\hat{a} = 0.0$ (blue circles) at least the fluxes in the (2,1)-mode (top middle panel) and in the (3,3)-mode (bottom middle panel) are reasonable.

Another useful information that one reads off Fig. 2 regards the spin-dependence of the multipolar fluxes at fixed radius. One finds that, for each value of $\hat{a}$ and for each multipole, each data set in Fig. 2 can be accurately fitted with a polynomial in σ. More precisely, for weak-field orbits the σ-dependence is essentially linear. By contrast, for strong-field orbits the polynomial can be of higher order, at most third order. This is interpreted as a direct reflection of the Tulczyjew-SSC, Eq. (8), and the related σ-squared dependence of the dynamics, in connection with the fact that the TE source term is linear in the spin. The appearance of the Riemann-tensor in connection with the $\mathcal{O}(\sigma^2)$ terms in Eq. (8) explains the transition to completely linear spin dependence in the weak-field.

As a final comment we mention that one cannot directly contrast these plots with the numbers stated in Tables II–IV because the latter refer to the PN-formulas recast in terms of x. While it is possible to compute all the relevant quantities, i.e. $F_{S_{\ell m}}$, $\hat{F}_{S_{\ell m}}$, $\eta_{\ell m}$ and $\hat{\eta}_{\ell m}$, from one another in our numerical data the analytical predictions are not strictly equivalent because of the approximation of Ω, see discussion in Sec. IV B. Though the general trend is the same, the values of
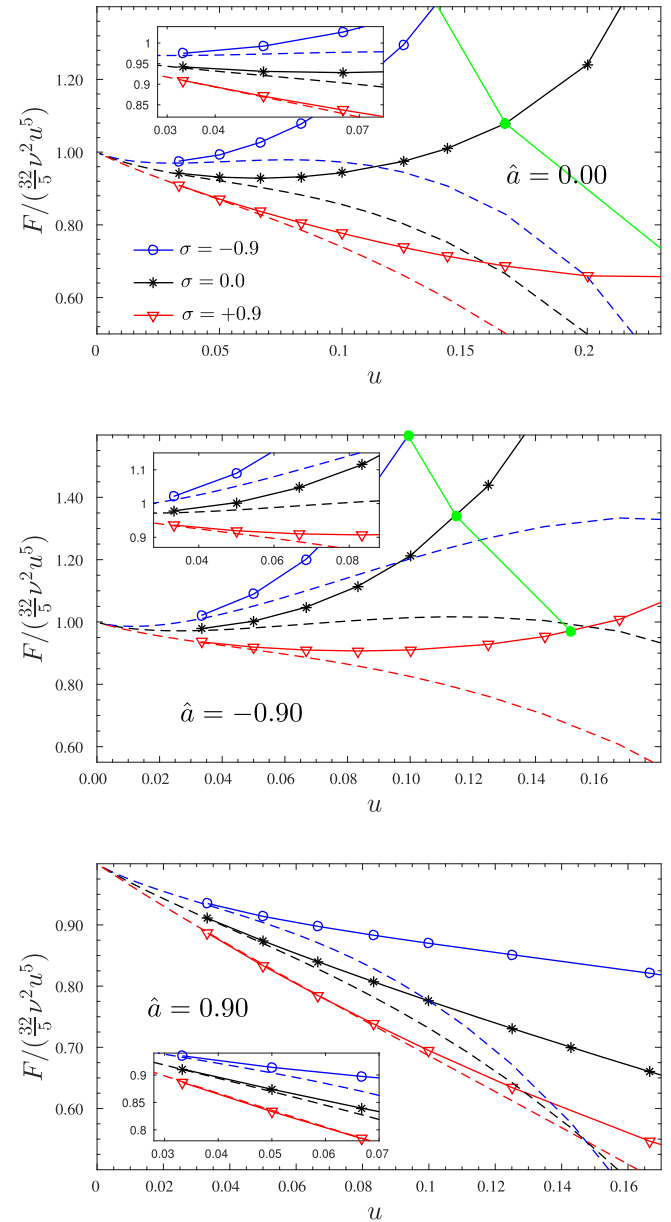
FIG. 3. Comparison of numerical (solid) and analytical PN (dashed) total energy fluxes over $u \equiv M/r$. Compare with Fig. 1 for further descriptions. In all three panels, i.e. for all considered background spins $\hat{a} = 0.0$ (top panel), $\hat{a} = -0.9$ (middle panel), and $\hat{a} = +0.9$ (bottom panel), we observe an unambiguous trend of our numerical data, approximated as the sum of $m = 1, 2, 3$-modes, towards the 2.5PN prediction of Tanaka *et al.* [51] as $u \to 0$.

fractional differences shown in Tables II–IV are not fully compatible with what one would obtain from the data corresponding to Fig. 2.

3. Total flux with respect to *u*

For completeness, we repeat the consistency check for the total energy flux as obtained from our numerical results and the 2.5PN predictions in terms of $u \equiv M/r$. This means we normalize our full flux here by $32/5u^5$ instead of using the conventional Newtonian flux $32/5x^5$. The relevant 2.5PN prediction of [51] is Eq. (32) above.

Figure 3 compares the fluxes for the three background spins $\hat{a} = 0.0$ (top panel), $\hat{a} = -0.9$ (middle panel), and $\hat{a} = +0.9$ (bottom panel) and the three values of the particle spin $\sigma = -0.9$ (blue, circles), $\sigma = 0.0$ (black, stars), $\sigma = 0.9$ (red, triangles). In all cases there is a clear trend of the numerical results (solid lines) toward the analytical predictions (dashed lines). In fact, comparing with Fig. 1 the agreement seems to be even more pronounced in this comparison over *u*. This must be mainly attributed to the pure visual effect that originates from the larger separation of the dashed lines from one another in this representation. On the contrary computing the fractional differences between our numerics and the PN formula, Eq. (32), we find rather larger than smaller differences compared to Tables II–IV. For example, at $\hat{a} = -0.9$ and $\hat{r} = 20$ we find numerically for $\sigma = -0.9$ that $F_{m\leq3}/(\frac{32}{5}u^5) = 1.089$, which is $\sim 3.5\%$ off the PN prediction 1.0510, and for $\sigma = +0.9$ we find $F_{m\leq3}/(\frac{32}{5}u^5) = 0.9193$, which is $\sim 0.91\%$ off the PN prediction 0.9109. Overall, this complementary comparison of the total energy flux confirms as well, visually even more pronouncedly, a clear convergence of the numerical results toward the PN predictions.

4. Cross-check against [Phys. Rev. D 82, 084013 (2010)]

Apart from the 2.5PN analytical prediction, we can compare our numerical results for the flux in the S_{-222}-mode with the numerical results of [44], in which the multipolar energy fluxes from a spinning particle on a CEO are computed by solving the TE in the frequency domain. In that study, the dynamics are obtained within the same approximations that we use, i.e. solving the MPEQs with the TUL-SSC. As checked in Sec. II, our dynamics agree at least in the orbital frequency with that of [44], which is a convincing indication that we are, in fact, considering the same physical system.

We can make a direct comparison for $\hat{r} = 10$, $\hat{a} = 0$, in which case the (*not* Newton-normalized) S_{-222}-flux
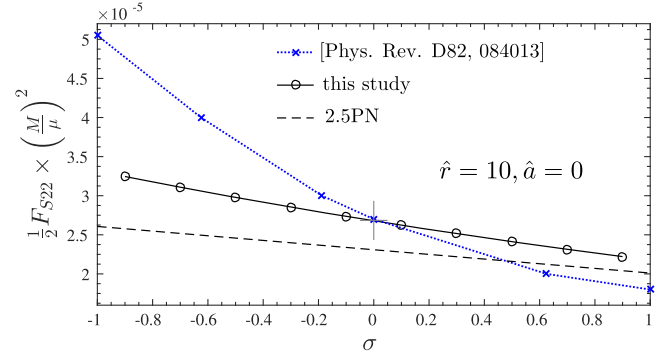

FIG. 4. Cross-check of the energy flux in the S_{-222}- = mode as obtained in this study (black solid, circles) against the results of [44] (blue dotted, crosses), at $\hat{r} = 10$ and for $\hat{a} = 0.0$. The 2.5PN prediction is included for completeness (black dashed). The data marked by crosses were extracted visually by inspecting the top right panel in Fig. 4 in [44]. Note that here we show the *not* Newton-normalized fluxes. The data points of [44] disagree qualitatively with both our numerical data and the 2.5PN accurate analytical flux. Note that we have indications that the underlying dynamics is the same in both cases. Both numerical solutions are consistent with one another at $\sigma = 0.0$ and also with the frequency-domain data of [84], which is marked by the small gray cross.

we considered was shown versus the particle spin σ in Fig. 4 of [44]. Our Fig. 4 draws a visual comparison between the results as: (i) obtained by [44], represented as crosses joined by a dotted line, (ii) as computed with our numerical code; (iii) as obtained from the 2.5 PN approximate formula $F_{S_{22}}/\nu^2 = 32/5u^5\hat{\eta}_{22}$. Note that in [44] the $m = \pm 2$ contributions were not summed together so that we need to compare it with $F_{S_{22}}/2$. Moreover, the data for the crosses joined by the dotted line was read off directly from Fig. 4 in [44]. The errors made in extracting the points from the plot are expected to be small in comparison to the differences we discuss below. Our Fig. 4 shows that the results of [44] (blue dotted, crosses) are in *quantitative* disagreement with both the post-Newtonian formula (black, dashed) and our numerical computations (black solid, circles). The reasons for the disagreement are unclear at the moment. Nevertheless, we are convinced of the correctness of our implementation because of the consistency with the 2.5PN expressions, which was not shown in [44]. Furthermore, note that the nonlinear shape of the blue dotted line with crosses (the numerical results of [44]) resembles qualitatively what we find for the 22-mode at smaller radii; e.g., see the top right panel of Fig. 2, whose blue line shows our results for $\hat{a} = 0.0$ at $\hat{r} = 5$ and is nonlinear in a similar way.

APPENDIX B: DATA TABLES

TABLE II. Case $\hat{a} = 0$: fractional differences between numerical and PN energy fluxes $1 - F^{\text{PN}}/F^{\text{Num}}$. From left to right, the columns report: the dimensionless Boyer-Lindquist orbital radius $\hat{r}$; the dimensionless orbital frequency $\hat{\Omega}$; the PN-parameter $x = \hat{\Omega}^{2/3}$; the, Newton-normalized, total numerical flux $\hat{F}^{\text{Num}}_{(m \leq 3)}$ summed over $m = 1, 2, 3$; the corresponding fractional difference with the 2.5 PN result, Eq. (35) the $\ell = m = 2$ numerical contribution; $\hat{F}^{\text{Num}}_{22}$; the fractional difference with the corresponding PN result, Eq. (37); and the analogous columns for $\ell = 2$, $m = 1$ and $\ell = m = 3$.

							$\hat{a} = 0.00$				
$\hat{r}$	σ	$M\Omega$	x	$\hat{F}_{m \leq 3}$	$\Delta\hat{F}_{m \leq 3}[\%]$	$\hat{F}_{S22}$	$\Delta\hat{F}_{S22}[\%]$	$\hat{F}_{S21}$	$\Delta\hat{F}_{S21}[\%]$	$\hat{F}_{S33}$	$\Delta\hat{F}_{S33}[\%]$
4.00	−0.90	0.150524	0.282968	3.1651	99.49	2.2085	142.28	2.1513	9.75	2.4164	18.06
	−0.50	0.138047	0.267107	2.4858	96.74	1.7912	138.97	2.2948	27.12	1.8241	8.32
	0.00	0.125000	0.250000	1.8220	95.55	1.3624	135.08	2.2378	33.78	1.2637	7.32
	0.50	0.114518	0.235821	1.3433	87.11	1.0396	131.00	2.0934	32.59	0.8677	26.81
	0.90	0.107796	0.226500	1.0750	82.60	0.8516	127.49	2.0062	29.44	0.6524	42.38
5.00	−0.90	0.101836	0.218072	1.5795	67.31	1.2118	102.08	0.9497	38.51	1.2152	19.31
	−0.50	0.095924	0.209549	1.4241	64.21	1.1119	96.38	1.2456	3.58	1.0572	20.66
	0.00	0.089443	0.200000	1.2409	58.93	0.9885	89.46	1.5479	14.78	0.8771	23.82
	0.50	0.083900	0.191650	1.0702	54.46	0.8683	82.53	1.7693	20.80	0.7157	28.88
	0.90	0.080095	0.185810	0.9530	50.07	0.7831	77.04	1.9220	22.13	0.6088	32.55
6.00	−0.90	0.074985	0.177821	1.2515	43.27	1.0117	65.68	0.7009	42.85	0.9752	22.37
	−0.50	0.071724	0.172628	1.1731	41.23	0.9590	62.03	0.9790	11.12	0.8854	21.81
	0.00	0.068041	0.166667	1.0788	36.08	0.8927	57.41	1.3231	7.40	0.7814	21.48
	0.50	0.064772	0.161284	0.9836	34.69	0.8231	52.45	1.6346	15.02	0.6815	22.30
	0.90	0.062438	0.157386	0.9142	31.66	0.7710	48.46	1.8745	18.07	0.6112	22.59
7.00	−0.90	0.058275	0.150310	1.1203	28.62	0.9369	43.31	0.6051	36.22	0.8833	19.24
	−0.50	0.056286	0.146871	1.0700	27.30	0.9016	41.05	0.8663	11.89	0.8211	18.19
	0.00	0.053995	0.142857	1.0097	22.96	0.8577	38.14	1.2148	4.04	0.7488	16.85
	0.50	0.051910	0.139156	0.9462	23.02	0.8097	34.78	1.5577	11.63	0.6765	16.39
	0.90	0.050385	0.136416	0.8990	21.00	0.7733	32.07	1.8364	15.39	0.6244	15.70
8.00	−0.90	0.047019	0.130271	1.0534	19.64	0.9024	29.69	0.5603	28.04	0.8406	15.52
	−0.50	0.045716	0.127854	1.0174	18.76	0.8760	28.23	0.8085	10.73	0.7932	14.41
	0.00	0.044194	0.125000	0.9745	15.18	0.8438	26.38	1.1527	2.33	0.7382	12.84
	0.50	0.042785	0.122329	0.9279	15.87	0.8076	24.04	1.5063	9.41	0.6816	12.05
	0.90	0.041737	0.120322	0.8931	14.50	0.7801	22.18	1.8029	13.45	0.6403	11.11
10.00	−0.90	0.033041	0.102968	0.9909	10.17	0.8762	15.47	0.5266	15.06	0.8087	9.84
	−0.50	0.032394	0.101619	0.9688	9.73	0.8591	14.79	0.7566	7.63	0.7769	8.93
	0.00	0.031623	0.100000	0.9432	7.28	0.8389	13.99	1.0865	0.85	0.7405	7.51
	0.50	0.030893	0.098456	0.9137	8.28	0.8149	12.72	1.4394	6.72	0.7009	6.77
	0.90	0.030339	0.097275	0.8919	7.58	0.7970	11.77	1.7453	10.81	0.6720	5.92
12.00	−0.90	0.024867	0.085196	0.9648	5.79	0.8706	8.97	0.5210	7.12	0.8028	6.42
	−0.50	0.024499	0.084354	0.9494	5.55	0.8582	8.60	0.7380	5.20	0.7791	5.72
	0.00	0.024056	0.083333	0.9321	3.79	0.8440	8.24	1.0533	0.32	0.7524	4.56
	0.50	0.023631	0.082349	0.9110	4.73	0.8263	7.45	1.3959	5.15	0.7220	4.04
	0.90	0.023304	0.081587	0.8957	4.34	0.8133	6.90	1.6974	9.06	0.7000	3.37
15.00	−0.90	0.017624	0.067724	0.9492	2.81	0.8738	4.53	0.5290	0.91	0.8085	3.64
	−0.50	0.017439	0.067248	0.9390	2.68	0.8651	4.36	0.7318	2.93	0.7917	3.18
	0.00	0.017213	0.066667	0.9281	1.55	0.8559	4.29	1.0276	0.04	0.7733	2.31
	0.50	0.016994	0.066100	0.9135	2.28	0.8432	3.79	1.3515	3.75	0.7507	2.04
	0.90	0.016824	0.065658	0.9033	2.09	0.8342	3.52	1.6394	7.32	0.7347	1.59
20.00	−0.90	0.011352	0.050511	0.9433	1.00	0.8858	1.81	0.5537	3.00	0.8266	1.69
	−0.50	0.011275	0.050282	0.9370	0.94	0.8802	1.74	0.7396	1.04	0.8156	1.43
	0.00	0.011180	0.050000	0.9312	0.32	0.8750	1.83	1.0090	0.06	0.8042	0.81
	0.50	0.011088	0.049723	0.9215	0.78	0.8663	1.52	1.3048	2.59	0.7884	0.79
	0.90	0.011015	0.049504	0.9153	0.70	0.8606	1.41	1.5682	5.63	0.7777	0.54
30.00	−0.90	0.006136	0.033517	0.9485	0.23	0.9088	0.53	0.5989	3.84	0.8601	0.47
	0.00	0.006086	0.033333	0.9420	0.14	0.9026	0.55	0.9972	0.06	0.8476	0.06
	0.90	0.006036	0.033152	0.9341	0.14	0.8952	0.42	1.4652	3.22	0.8323	0.002

TABLE III.   Case $\hat{a} = -0.9$. Compare caption of Table II for general descriptions. Note the square brackets around all stated values concerning the multipolar fluxes for $\sigma \neq 0$ at $\hat{r} = 30$. These values in brackets refer to multipolar fluxes with respect to the $Y_{-2\ell m}$ decomposition, whereas the table otherwise states values with respect to the $S_{-2\ell m}$ basis. The reason is that at very large radii we did not compute the $S_{-2\ell m}$-fluxes accurately, as discussed in Sec. IV A. The comparison with the analytical formulas, which refer to the $S_{-2\ell m}$ decomposition, is nonetheless valid because for the stated modes, at such low frequencies, we verified that $S_{-2\ell m} \simeq Y_{-2\ell m}$.

						$\hat{a} = -0.90$					
$\hat{r}$	σ	$M\Omega$	x	$\hat{F}_{m\leq 3}$	$\Delta\hat{F}_{m\leq 3}[\%]$	$\hat{F}_{S22}$	$\Delta\hat{F}_{S22}[\%]$	$\hat{F}_{S21}$	$\Delta\hat{F}_{S21}[\%]$	$\hat{F}_{S33}$	$\Delta\hat{F}_{S33}[\%]$
5.00	−0.90	0.117709	0.240182	6.4781	84.00	4.4357	94.93	13.2093	82.52	5.7381	64.47
	−0.50	0.107980	0.226757	4.6611	80.14	3.3073	92.63	10.7512	76.25	3.9652	55.31
	0.00	0.097273	0.211509	3.1231	70.36	2.3101	88.77	8.4271	65.51	2.5068	40.50
	0.50	0.088022	0.197877	2.1067	65.70	1.6213	83.45	6.6711	50.56	1.5675	19.55
	0.90	0.081574	0.188091	1.5575	57.43	1.2332	77.96	5.6404	35.65	1.0789	2.54
6.00	−0.90	0.083178	0.190548	2.5692	57.56	1.9524	69.67	4.7113	60.49	2.2341	29.84
	−0.50	0.078170	0.182821	2.2155	54.79	1.7145	67.21	4.8787	54.96	1.8580	24.13
	0.00	0.072480	0.173838	1.8252	45.13	1.4441	63.39	4.9193	46.51	1.4529	14.90
	0.50	0.067380	0.165585	1.4840	44.41	1.1997	58.43	4.7967	35.89	1.1107	2.14
	0.90	0.063698	0.159496	1.2557	38.76	1.0312	53.74	4.6663	26.39	0.8907	10.26
7.00	−0.90	0.063048	0.158409	1.7770	38.87	1.4272	48.27	3.0020	46.35	1.5407	14.43
	−0.50	0.060132	0.153487	1.6183	37.11	1.3152	46.66	3.3610	41.14	1.3550	10.54
	0.00	0.056753	0.147681	1.4326	28.96	1.1805	44.10	3.7271	34.52	1.1454	4.61
	0.50	0.053653	0.142253	1.2543	30.30	1.0474	40.56	3.9731	26.93	0.9528	3.49
	0.90	0.051364	0.138178	1.1260	26.61	0.9494	37.27	4.1277	20.72	0.8195	10.92
8.00	−0.90	0.050040	0.135792	1.4629	26.85	1.2185	33.83	2.3078	37.00	1.2643	7.29
	−0.50	0.048194	0.132432	1.3683	25.72	1.1487	32.82	2.6880	31.89	1.1465	4.52
	0.00	0.046025	0.128428	1.2557	19.06	1.0639	31.19	3.1322	26.58	1.0114	0.56
	0.50	0.044003	0.124640	1.1424	21.22	0.9764	28.73	3.5031	21.06	0.8815	4.91
	0.90	0.042488	0.121762	1.0584	18.76	0.9103	26.48	3.7752	16.95	0.7886	9.70
10.00	−0.90	0.034471	0.105918	1.2058	13.93	1.0499	17.92	1.7209	25.90	1.0416	2.12
	−0.50	0.033596	0.104117	1.1578	13.41	1.0122	17.49	2.0786	20.85	0.9771	0.55
	0.00	0.032549	0.101944	1.1008	8.92	0.9667	16.84	2.5386	17.14	0.9023	1.43
	0.50	0.031554	0.099855	1.0401	11.26	0.9174	15.55	2.9757	14.06	0.8261	4.37
	0.90	0.030794	0.098245	0.9943	10.08	0.8798	14.45	3.3271	12.33	0.7703	6.74
12.00	−0.90	0.025653	0.086981	1.1021	7.94	0.9850	10.43	1.4703	19.75	0.9567	0.78
	−0.50	0.025171	0.085888	1.0719	7.67	0.9602	10.22	1.8006	14.82	0.9136	0.23
	0.00	0.024589	0.084558	1.0364	4.50	0.9307	9.98	2.2403	11.97	0.8640	1.33
	0.50	0.024028	0.083269	0.9969	6.52	0.8974	9.20	2.6788	10.17	0.8111	3.22
	0.90	0.023595	0.082266	0.9673	5.88	0.8724	8.61	3.0449	9.67	0.7724	4.59
15.00	−0.90	0.018005	0.068697	1.0332	3.87	0.9458	5.26	1.2932	14.70	0.9066	0.37
	−0.50	0.017771	0.068098	1.0148	3.75	0.9303	5.20	1.5866	9.80	0.8786	0.26
	0.00	0.017484	0.067364	0.9939	1.72	0.9121	5.19	1.9920	7.72	0.8471	0.77
	0.50	0.017205	0.066647	0.9691	3.22	0.8903	4.73	2.4058	6.81	0.8116	1.94
	0.90	0.016988	0.066084	0.9509	2.92	0.8743	4.45	2.7625	7.24	0.7855	2.71
20.00	−0.90	0.011504	0.050961	0.9905	1.42	0.9277	2.12	1.1811	11.57	0.8892	0.85
	−0.50	0.011410	0.050682	0.9802	1.37	0.9182	2.07	1.4296	6.55	0.8699	0.25
	0.00	0.011294	0.050338	0.9694	0.27	0.9085	2.21	1.7768	4.40	0.8493	0.18
	0.50	0.011180	0.049999	0.9545	1.18	0.8955	1.97	2.1721	5.20	0.8259	1.00
	0.90	0.011090	0.049732	0.9444	1.07	0.8846	1.70	2.4992	6.13	0.8225	0.16
30.00	−0.90	0.006179	0.033672	0.9708	0.33	[0.9291]	[0.59]	[1.067]	[5.92]	[0.8900]	[0.45]
	0.00	0.006119	0.033456	0.9607	0.23	0.9196	0.66	1.5795	2.00	0.8710	0.15
	0.90	0.006061	0.033243	0.9491	0.25	[0.9086]	[0.55]	[2.148]	[2.80]	[0.8500]	[0.44]

TABLE IV. Case $\hat{a} = 0.9$. Compare caption of Table II for description. Additionally, in this table there appear configurations that are, as yet, not covered by our experiments. These are marked with the ×-symbol. Furthermore, note the square brackets around all stated values concerning the multipolar fluxes for $\sigma \neq 0$ at $\hat{r} = 30$. These values in brackets refer to multipolar fluxes with respect to the $Y_{-2\ell m}$ decomposition, whereas the table otherwise states values with respect to the $S_{-2\ell m}$ basis. The reason is that at very large radii we did not compute the $S_{-2\ell m}$-fluxes accurately, as discussed in Sec. IV A. The comparison with the analytical formulas, which refer to the $S_{-2\ell m}$ decomposition, is nonetheless valid because for the stated modes, at such low frequencies, we verified that $S_{-2\ell m} \simeq Y_{-2\ell m}$.

							$\hat{a} = 0.90$				
$\hat{r}$	σ	Ω	x	$\hat{F}_{m\leq3}$	$\Delta\hat{F}_{m\leq3}[\%]$	$\hat{F}_{S22}$	$\Delta\hat{F}_{S22}[\%]$	$\hat{F}_{S21}$	$\Delta\hat{F}_{S21}[\%]$	$\hat{F}_{S33}$	$\Delta\hat{F}_{S33}[\%]$
4.00	−0.90	0.124009	0.248677	0.7725	124.37	0.6023	224.00	0.0004	469114.18	0.5038	145.45
	−0.50	0.118248	0.240914	0.7657	111.89	0.6063	193.82	0.0311	3703.59	0.4873	116.16
	0.00	0.112360	0.232848	0.7561	112.04	0.6070	164.26	0.1451	334.74	0.4667	82.26
	0.50	0.107776	0.226472	0.7427	89.70	0.6024	141.41	0.3058	47.12	0.4443	50.82
	0.90	0.104933	0.222472	0.7355	83.57	0.6001	126.34	0.4618	137.58	0.4299	24.94
6.00	−0.90	0.068067	0.166708	0.8200	38.65	0.6886	65.27	×	×	0.5809	52.87
	−0.50	0.066199	0.163645	0.8125	35.78	0.6866	58.84	×	×	0.5654	41.44
	0.00	0.064115	0.160192	0.8047	35.16	0.6841	51.74	0.2229	110.39	0.5478	27.08
	0.50	0.062293	0.157142	0.7933	29.68	0.6777	45.23	×	×	0.5277	13.59
	0.90	0.061011	0.154978	0.7860	27.66	0.6736	40.61	0.6288	61.86	0.5137	2.36
8.00	−0.90	0.044299	0.125197	0.8447	16.51	0.7370	27.42	0.0320	1329.22	0.6339	25.20
	−0.50	0.043468	0.123627	0.8385	15.42	0.7339	25.08	×	×	0.6205	19.11
	0.00	0.042504	0.121792	0.8325	14.81	0.7310	22.47	0.2835	52.23	0.6059	11.21
	0.50	0.041619	0.120096	0.8229	12.94	0.7246	19.71	×	×	0.5881	3.97
	0.90	0.040966	0.118837	0.8169	12.05	0.7205	17.74	0.7217	38.38	0.5758	2.15
10.00	−0.90	0.031712	0.100188	0.8618	8.36	0.7701	13.96	0.0590	433.26	0.6736	13.97
	−0.50	0.031271	0.099256	0.8566	7.83	0.7670	12.85	×	×	0.6621	10.22
	0.00	0.030748	0.098147	0.8520	7.33	0.7643	11.69	0.3319	29.76	0.6499	5.20
	0.50	0.030256	0.097097	0.8438	6.57	0.7582	10.20	×	×	0.6342	0.80
	0.90	0.029884	0.096300	0.8388	6.10	0.7545	9.19	0.7794	27.41	0.6234	3.00
12.00	−0.90	0.024124	0.083489	0.8749	4.70	0.7948	8.00	×	×	0.7048	8.55
	−0.50	0.023861	0.082883	0.8705	4.40	0.7919	7.40	×	×	0.6948	6.02
	0.00	0.023546	0.082152	0.8669	4.00	0.7895	6.83	0.3716	18.98	0.6846	2.53
	0.50	0.023246	0.081451	0.8597	3.67	0.7839	5.89	×	×	0.6705	0.37
	0.90	0.023015	0.080911	0.8554	3.39	0.7805	5.30	0.8184	21.18	0.6613	2.99
15.00	−0.90	0.017257	0.066780	0.8900	2.23	0.8225	4.01	0.1257	70.13	0.7412	4.63
	−0.50	0.017119	0.066423	0.8864	2.08	0.8199	3.71	×	×	0.7326	3.11
	0.00	0.016951	0.065987	0.8839	1.79	0.8181	3.53	0.4197	11.06	0.7248	0.80
	0.50	0.016788	0.065564	0.8777	1.70	0.8130	2.96	×	×	0.7127	0.89
	0.90	0.016662	0.065235	0.8743	1.55	0.8100	2.64	0.8574	15.69	0.7046	2.46
20.00	−0.90	0.011204	0.050069	0.9077	0.75	0.8552	1.71	0.1830	17.94	0.7862	1.83
	−0.50	0.011143	0.049889	0.9051	0.68	0.8519	1.45	0.3051	13.03	0.7799	0.98
	0.00	0.011069	0.049667	0.9037	0.53	0.8509	1.50	0.4797	5.60	0.7723	0.11
	0.50	0.010996	0.049450	0.8986	0.51	0.8461	1.11	0.7000	4.49	0.7631	0.98
	0.90	0.010939	0.049279	0.8961	0.45	0.8444	1.05	0.9177	13.00	0.7577	1.93
30.00	−0.90	0.006094	0.033365	0.9306	0.16	[0.8924]	[0.46]	[0.2722]	[0.64]	[0.8381]	[0.52]
	0.00	0.006053	0.033212	0.9275	0.02	0.8896	0.45	0.5585	2.20	0.8296	0.36
	0.90	0.006012	0.033062	0.9234	0.08	[0.8856]	[0.31]	[0.9262]	[5.95]	[0.8190]	[0.99]

[1] T. Regge and J. A. Wheeler, Stability of a Schwarzschild singularity, Phys. Rev. **108**, 1063 (1957).

[2] F. J. Zerilli, Effective Potential for Even Parity Regge-Wheeler Gravitational Perturbation Equations, Phys. Rev. Lett. **24**, 737 (1970).

[3] S. A. Teukolsky, Rotating Black Holes—Separable Wave Equations for Gravitational and Electromagnetic Perturbations, Phys. Rev. Lett. **29**, 1114 (1972).

[4] S. A. Teukolsky, Perturbations of a rotating black hole. 1. Fundamental equations for gravitational electromagnetic

and neutrino field perturbations, Astrophys. J. **185**, 635 (1973).

[5] L. Barack and C. Cutler, LISA capture sources: Approximate waveforms, signal-to-noise ratios, and parameter estimation accuracy, Phys. Rev. D **69**, 082005 (2004).

[6] A. L. Tiec, The overlap of numerical relativity, perturbation theory and post-Newtonian theory in the binary black hole problem, Int. J. Mod. Phys. D **23**, 1430022 (2014).

[7] T. Dietrich and S. Bernuzzi, Simulations of rotating neutron star collapse with the puncture gauge: end state and gravitational waveforms, Phys. Rev. D **91**, 044039 (2015).

[8] A. Nagar, Gravitational recoil in nonspinning black hole binaries: The span of test-mass results, Phys. Rev. D **88**, 121501 (2013).

[9] T. Damour and A. Nagar, The effective one body description of the two-body problem, arXiv:0906.1769.

[10] T. Dietrich, N. Moldenhauer, N. K. Johnson-McDaniel, S. Bernuzzi, C. M. Markakis, B. Bruegmann, and W. Tichy, Binary neutron stars with generic spin, eccentricity, mass ratio, and compactness—quasi-equilibrium sequences and first evolutions, Phys. Rev. D **92**, 124007 (2015).

[11] J. Frenkel, Die elektrodynamik des rotierenden elektrons, Z. Phys. **37**, 243 (1926).

[12] C. Lanczos, Ueber eine invariante formulierung der erhaltungssaetze in der allgemeinen relativitaetstheorie, Z. Phys. **59**, 514 (1930).

[13] M. Mathisson, Neue mechanik materieller systemes, Acta Phys. Pol. **6**, 163 (1937).

[14] M. Mathisson, Republication of: New mechanics of material systems, Gen. Relativ. Gravit. **42**, 1011 (2010).

[15] W Tulczyjew, Motion of multipole particles in general relativity theory, Acta Phys. Pol. **18**, 393 (1959).

[16] J. Steinhoff, Canonical formulation of spin in general relativity, Ann. Phys. (Berlin) **523**, 296 (2011).

[17] A. Papapetrou, Spinning test particles in general relativity. 1., Proc. R. Soc. A **209**, 248 (1951).

[18] E. Corinaldesi and A. Papapetrou, Spinning test particles in general relativity. 2., Proc. R. Soc. A **209**, 259 (1951).

[19] W. G. Dixon, A covariant multipole formalism for extended test bodies in general relativity, Il Nuovo Cimento **34**, 317 (1964).

[20] W. G. Dixon, Dynamics of extended bodies in general relativity. I. Momentum and angular momentum, Proc. R. Soc. A **314**, 499 (1970).

[21] W. G. Dixon, Dynamics of extended bodies in general relativity. II. Moments of the charge-current vector, Proc. R. Soc. A **319**, 509 (1970).

[22] W. G Dixon, Dynamics of extended bodies in general relativity. iii. Equations of motion, Phil. Trans. R. Soc. A **277**, 59 (1974).

[23] R. M. Wald, Gravitational spin interaction, Phys. Rev. D **6**, 406 (1972).

[24] C Moller, Sur la dynamique des systemes ayant un moment angulaire interne, Ann Inst. Henri Poincaré **11**, 251 (1949).

[25] W. Beiglboeck, The center-of-mass in einsteins theory of gravitation, Commun. Math. Phys. **5**, 106 (1967).

[26] M. H. L. Pryce, The mass center in the restricted theory of relativity and its connection with the quantum theory of elementary particles, Proc. R. Soc. A **195**, 62 (1948).

[27] T. D. Newton and E. P. Wigner, Localized states for elementary systems, Rev. Mod. Phys. **21**, 400 (1949).

[28] F. A. E. Pirani, On the physical significance of the Riemann tensor, Acta Phys. Pol. **15**, 389 (1956).

[29] K Kyrian and O Semerak, Spinning test particles in a Kerr field, Mon. Not. R. Astron. Soc. **382**, 1922 (2007).

[30] O. Semerak, Spinning test particles in a Kerr field. 1., Mon. Not. R. Astron. Soc. **308**, 863 (1999).

[31] D. Bini, G. Gemelli, and R. Ruffini, Spinning test particles in general relativity: Nongeodesic motion in the Reissner-Nordstrom space-time, Phys. Rev. D **61**, 064013 (2000).

[32] M. D. Hartl, Dynamics of spinning test particles in Kerr space-time, Phys. Rev. D **67**, 024005 (2003).

[33] M. D. Hartl, A survey of spinning test particle orbits in Kerr space-time, Phys. Rev. D **67**, 104023 (2003).

[34] J. Ehlers and E. Rudolph, Dynamics of extended bodies in general relativity center-of-mass description and quasirigidity, Gen. Relativ. Gravit. **8**, 197 (1977).

[35] T. Hinderer, A. Buonanno, A. H. Mroué, D. A. Hemberger, G. Lovelace *et al.*, Periastron advance in spinning black hole binaries: Comparing effective-one-body and numerical relativity, Phys. Rev. D **88**, 084005 (2013).

[36] D. Bini, P. Fortini, A. Geralico, and A. Ortolan, Quadrupole effects on the motion of extended bodies in Kerr spacetime, Classical Quantum Gravity **25**, 125007 (2008).

[37] D. Bini and A. Geralico, Deviation of quadrupolar bodies from geodesic motion in a Kerr spacetime, Phys. Rev. D **89**, 044013 (2014).

[38] D. Bini and A. Geralico, Dynamics of quadrupolar bodies in a Schwarzschild spacetime, Phys. Rev. D **87**, 024028 (2013).

[39] D. Bini and A. Geralico, Effect of an arbitrary spin orientation on the quadrupolar structure of an extended body in a Schwarzschild spacetime, Phys. Rev. D **91**, 104036 (2015).

[40] E. A. Huerta and J. R Gair, Importance of including small body spin effects in the modelling of extreme and intermediate mass-ratio inspirals, Phys. Rev. D **84**, 064023 (2011).

[41] Y. Mino, M. Shibata, and T. Tanaka, Gravitational waves induced by a spinning particle falling into a rotating black hole, Phys. Rev. D **53**, 622 (1996).

[42] M. Sasaki and T. Nakamura, Gravitational radiation from a Kerr black hole. 1. Formulation and a method for numerical analysis, Prog. Theor. Phys. **67**, 1788 (1982).

[43] M. Saijo, K.-i. Maeda, M. Shibata, and Y. Mino, Gravitational waves from a spinning particle plunging into a Kerr black hole, Phys. Rev. D **58**, 064005 (1998).

[44] W.-B. Han, Gravitational radiations from a spinning compact object around a supermassive Kerr black hole in circular orbit, Phys. Rev. D **82**, 084013 (2010).

[45] K. Tominaga, M. Saijo, and K.-i. Maeda, Gravitational waves from a spinning particle scattered by a relativistic star: Axial mode case, Phys. Rev. D **63**, 124012 (2001).

[46] K. Tominaga, M. Saijo, and K.-i. Maeda, Gravitational waves from a test particle scattered by a neutron star: Axial mode case, Phys. Rev. D **60**, 024004 (1999).

[47] L. M. Burko and G. Khanna, Self-force gravitational waveforms for extreme and intermediate mass ratio inspirals. III: Spin-orbit coupling revisited, Phys. Rev. D **91,** 104017 (2015).

[48] L. E. Kidder, C. M. Will, and A. G. Wiseman, Spin effects in the inspiral of coalescing compact binaries, Phys. Rev. D **47,** R4183 (1993).

[49] L. E. Kidder, Coalescing binary systems of compact objects to post-Newtonian 5/2 order. 5. Spin effects, Phys. Rev. D **52,** 821 (1995).

[50] L. Blanchet, T. Damour, B. R. Iyer, C. M. Will, and A. G. Wiseman, Gravitational Radiation Damping of Compact Binary Systems to Second Post-Newtonian Order, Phys. Rev. Lett. **74,** 3515 (1995).

[51] T. Tanaka, Y. Mino, M. Sasaki, and M. Shibata, Gravitational waves from a spinning particle in circular orbits around a rotating black hole. Phys. Rev. D **54,** 3762 (1996).

[52] A. Bohé, S. Marsat, and L. Blanchet, Next-to-next-to-leading order spin–orbit effects in the gravitational wave flux and orbital phasing of compact binaries, Classical Quantum Gravity **30,** 135009 (2013).

[53] S. Marsat, L. Blanchet, A. Bohe, and G. Faye, Gravitational waves from spinning compact object binaries: New post-Newtonian results, arXiv:1312.5375.

[54] L. Blanchet, A. Buonanno, and G. Faye, Tail-induced spin-orbit effect in the gravitational radiation of compact binaries, Phys. Rev. D **84,** 064041 (2011).

[55] Luc Blanchet, Alessandra Buonanno, and Guillaume Faye, Third post-Newtonian spin-orbit effect in the gravitational radiation flux of compact binaries, ASP Conf. Ser. **467,** 215 (2013).

[56] A. Bohé, G. Faye, S. Marsat, and E. K. Porter, Quadratic-in-spin effects in the orbital dynamics and gravitational-wave energy flux of compact binaries at the 3PN order, Classical Quantum Gravity **32,** 195010 (2015).

[57] S. Marsat, A. Bohé, L. Blanchet, and A. Buonanno, Next-to-leading tail-induced spin–orbit effects in the gravitational radiation flux of compact binaries, Classical Quantum Gravity **31,** 025023 (2014).

[58] T. Damour and A. Nagar, A new effective-one-body description of coalescing nonprecessing spinning black-hole binaries, Phys. Rev. D **90,** 044018 (2014).

[59] G. Lukes-Gerakopoulos, J. Seyrich, and D. Kunst, Investigating spinning test particles: spin supplementary conditions and the Hamiltonian formalism, Phys. Rev. D **90,** 104019 (2014).

[60] E. Harms, S. Bernuzzi, and B. Brügmann, Numerical solution of the $2+1$ Teukolsky equation on a hyperboloidal and horizon penetrating foliation of Kerr and application to late-time decays, Classical Quantum Gravity **30,** 115013 (2013).

[61] E. Harms, S. Bernuzzi, A. Nagar, and A. Zenginoğlu, A new gravitational wave generation algorithm for particle perturbations of the Kerr spacetime, Classical Quantum Gravity **31,** 245004 (2014).

[62] A. Nagar, E. Harms, S. Bernuzzi, and A. Zenginoglu, The antikick strikes back: recoil velocities for nearly-extremal binary black hole mergers in the test-mass limit, Phys. Rev. D **90,** 124086 (2014).

[63] T. Damour, B. R. Iyer, and A. Nagar, Improved resummation of post-Newtonian multipolar waveforms from circularized compact binaries, Phys. Rev. D **79,** 064004 (2009).

[64] Y. Pan, A. Buonanno, R. Fujita, E. Racine, and H. Tagoshi, Post-Newtonian factorized multipolar waveforms for spinning, non-precessing black-hole binaries, Phys. Rev. D **83,** 064003 (2011).

[65] Ryuichi Fujita, Gravitational waves from a particle in circular orbits around a rotating black hole to the 11th post-Newtonian order, Prog. Theor. Exp. Phys. **2015,** 033E01 (2015).

[66] G. Faye, L. Blanchet, and A. Buonanno, Higher-order spin effects in the dynamics of compact binaries. I. Equations of motion, Phys. Rev. D **74,** 104033 (2006).

[67] E. Barausse, E. Racine, and A. Buonanno, Hamiltonian of a spinning test-particle in curved spacetime, Phys. Rev. D **80,** 104025 (2009).

[68] E. Hackmann, C. Laemmerzahl, Y. N. Obukhov, D. Puetzfeld, and I. Schaffer, Motion of spinning test bodies in Kerr spacetime, Phys. Rev. D **90,** 064035 (2014).

[69] D. Bini and A. Geralico, Spin-geodesic deviations in the Kerr spacetime, Phys. Rev. D **84,** 104012 (2011).

[70] O. Semerák and M. Srámek, Spinning particles in vacuum spacetimes of different curvature types, Phys. Rev. D **92,** 064032 (2015).

[71] See also [59], where one of us studied systematically the differences between the MPEQs and the strictly linearized Hamiltonian approach of [67] and found deviations at high spin values.

[72] D. Bini, G. Faye, and A. Geralico, Dynamics of extended bodies in a Kerr spacetime with spin-induced quadrupole tensor, Phys. Rev. D **92,** 104003 (2015).

[73] J. Steinhoff and D. Puetzfeld, Influence of internal structure on the motion of test bodies in extreme mass ratio situations, Phys. Rev. D **86,** 044033 (2012).

[74] K. S. Thorne, Multipole expansions of gravitational radiation, Rev. Mod. Phys. **52,** 299 (1980).

[75] D. Bini and T. Damour, Two-body gravitational spin-orbit interaction at linear order in the mass ratio, Phys. Rev. D **90,** 024039 (2014).

[76] S. Suzuki and K.-i. Maeda, Innermost stable circular orbit of a spinning particle in Kerr space-time, Phys. Rev. D **58,** 023005 (1998).

[77] W.-B. Han and Z. Cao, Constructing EOB dynamics with numerical energy flux for intermediate-mass-ratio inspirals, Phys. Rev. D **84,** 044014 (2011).

[78] S. Bernuzzi, A. Nagar, and A. Zenginoğlu, Horizon-absorption effects in coalescing black-hole binaries: An effective-one-body study of the non-spinning case, Phys. Rev. D **86,** 104038 (2012).

[79] S. Bernuzzi, A. Nagar, and A. Zenginoğlu, Binary black hole coalescence in the large-mass-ratio limit: the hyperboloidal layer method and waveforms at null infinity, Phys. Rev. D **84,** 084026 (2011).

[80] S. Bernuzzi, A. Nagar, and A. Zenginoğlu, Binary black hole coalescence in the extreme-mass-ratio limit: testing and improving the effective-one-body multipolar waveform, Phys. Rev. D **83,** 064010 (2011).

[81] E. Barausse, A. Buonanno, S. A. Hughes, G. Khanna, S. O'Sullivan, and Y. Pan, Modeling multipolar gravitational-

wave emission from small mass-ratio mergers, Phys. Rev. D **85**, 024046 (2012).

[82] P. A. Sundararajan, G. Khanna, and S. A. Hughes, Binary black hole merger gravitational waves and recoil in the large mass ratio limit, Phys. Rev. D **81**, 104009 (2010).

[83] P. A. Sundararajan, G. Khanna, and S. A. Hughes, Towards adiabatic waveforms for inspiral into Kerr black holes: I. A new model of the source for the time domain perturbation equation, Phys. Rev. D **76**, 104005 (2007).

[84] S. A. Hughes, The evolution of circular, nonequatorial orbits of Kerr black holes due to gravitational wave emission, Phys. Rev. D **61**, 084004 (2000).

[85] A. Taracchini, A. Buonanno, G. Khanna, and S. A. Hughes, Small mass plunging into a Kerr black hole: Anatomy of the inspiral-merger-ringdown waveforms, Phys. Rev. D **90**, 084025 (2014).

[86] G. Calabrese, C. Gundlach, and D. Hilditch, Asymptotically null slices in numerical relativity: Mathematical analysis and spherical wave equation tests, Classical Quantum Gravity **23**, 4829 (2006).

[87] A. Zenginoğlu, Hyperboloidal foliations and scri-fixing, Classical Quantum Gravity **25**, 145002 (2008).

[88] A. Zenginoğlu and M. Tiglio, Spacelike matching to null infinity, Phys. Rev. D **80**, 024044 (2009).

[89] A. Zenginoğlu, Hyperboloidal layers for hyperbolic equations on unbounded domains, J. Comput. Phys. **230**, 2286 (2011).

[90] A. Vañó-Viñuales, S. Husa, and D. Hilditch, Spherical symmetry as a test case for unconstrained hyperboloidal evolution, Classical Quantum Gravity **32**, 175010 (2015).

[91] H. Yang, A. Zimmerman, A. Zenginoğlu, F. Zhang, E. Berti, and Y. Chen, Quasinormal modes of nearly extremal Kerr spacetimes: spectrum bifurcation and power-law ringdown, Phys. Rev. D **88**, 044047 (2013).

[92] M. Campanelli, G. Khanna, P. Laguna, J. Pullin, and M. P. Ryan, Perturbations of the Kerr space-time in horizon

[93] A.-K. Tornberg and B. Engquist, Numerical approximations of singular source terms in differential equations, J. Comput. Phys. **200**, 462 (2004).

[94] B. Engquist, A.-K. Tornberg, and R. Tsai, Discretization of Dirac delta functions in level set methods, J. Comput. Phys. **207**, 28 (2005).

[95] S. A. Hughes, Evolution of circular, nonequatorial orbits of Kerr black holes due to gravitational wave emission. 2. Inspiral trajectories and gravitational wave forms, Phys. Rev. D **64**, 064004 (2001).

[96] A. Taracchini, A. Buonanno, S. A. Hughes, and G. Khanna, Modeling the horizon-absorbed gravitational flux for equatorial-circular orbits in Kerr spacetime, Phys. Rev. D **88**, 044001 (2013).

[97] We have also obtained preliminary results for horizon fluxes, which will be discussed in a separate study.

[98] S. A. Teukolsky and W. H. Press, Perturbations of a rotating black hole. III—Interaction of the hole with gravitational and electromagnetic radiation, Astrophys. J. **193**, 443 (1974).

[99] R. Fujita, Gravitational waves from a particle in circular orbits around a Schwarzschild black hole to the 22nd post-Newtonian order, Prog. Theor. Phys. **128**, 971 (2012).

[100] A. G Shah, Gravitational-wave flux for a particle orbiting a Kerr black hole to 20th post-Newtonian order: A numerical approach, Phys. Rev. D **90**, 044025 (2014).

[101] B. Brügmann, A pseudospectral matrix method for time-dependent tensor fields on a spherical shell, J. Comput. Phys. **235**, 216 (2013).

[102] W. H. Press and S. A. Teukolsky, Perturbations of a rotating black hole. II. Dynamical stability of the Kerr metric, Astrophys. J. **185**, 649 (1973).